Geophysical Journal International

Geophys. J. Int. (2010) **182,** 137–154 doi: 10.1111/j.1365-246X.2010.04637.x

Temperature and heat flux scalings for isoviscous thermal convection in spherical geometry

Frédéric Deschamps, Paul J. Tackley and Takashi Nakagawa

Institute of Geophysics, Swiss Federal Institute of Technology Zurich, NO H9.3, Sonnegstrasse 5, 8092 Zurich, Switzerland.
E-mail: frederic.deschamps@erdw.ethz.ch

Accepted 2010 April 20. Received 2010 April 19; in original form 2009 November 27

SUMMARY

Parametrized convection, which has long been used to reconstruct the thermal history of planetary mantles, is based on scaling relationships between observables (including heat flux) and controlling parameters (the most important being the Rayleigh number, Ra). To explore the influence of spherical geometry on heat transfer, we have conducted two series of numerical experiments of thermal convection (one with bottom heating and the other with mixed heating) in an isoviscous spherical shell with various curvatures. Using these calculations and a generalized non-linear inversion, we then derive scaling laws for the average temperature and for the surface heat flux. In the case of bottom heating, we found that the non-dimensional average temperature is given by $\theta_m = f^2/(1+f^2)$, where f is the ratio between the core and total radii. The non-dimensional surface heat flux is fitted well by $Nu_{\rm top} = 0.36\, f^{0.32}\, Ra^{(0.273+0.05f)}\, \theta_m^{0.6}$. This scaling indicates that the available heating power decreases with increasing curvature (decreasing f). There exist strong trade-offs between the inverted parameters, that is, different sets of parameters explain our calculations well within error bars. For mixed heating, the non-dimensional average temperature and surface heat flux are well explained by $\theta_H = \theta_m + (1.68 - 0.8f)[(1+f+f^2)/3]^{0.79}\, h^{0.79}/Ra^{0.234}$, where h is the non-dimensional rate of internal heating, and $Nu_{\rm top} = 0.59\, f^{0.05}\, Ra^{(0.300-0.003f)}\, \theta_H^{1.23}$. Due to a competition between the radiogenic and convective powers, and for given values of h and Ra, there is a curvature for which the Urey ratio reaches a minimum. Applied to the Earth's mantle, the mixed heating scaling predicts a Urey ratio between 0.4 and 0.6, depending on the Rayleigh number. Additional parameters, including the thermal viscosity ratio, phase transitions, the presence of dense material in the deep mantle, and variability of the flow pattern in time, may enter an appropriate modelling of the Earth's mantle thermal history.

Key words: Mantle processes; Dynamics: convection currents, and mantle plumes; Heat generation and transport; Planetary interiors.

1 INTRODUCTION

Convection is the most efficient process of heat and mass transfer through planetary mantles. Reconstruction of the thermal history of planetary mantles requires a good description of the heat flux that can be accommodated by these mantles and released at the surface. A major difficulty in this reconstruction is that the Rayleigh number (the vigour of convection) is likely varying with time, either because mantle temperature was higher in the past (Archean Earth's mantle), or because the thickness of the convective layer increases with time (icy moons of giant planets). Furthermore, there still exist large uncertainties in the physical properties (e.g. the average viscosity, the thermal expansion, and the thermal diffusivity) of planetary mantles, and calculations with specific values of these parameters may not correctly describe the dynamics of these mantles. Despite the constant increase in computational power, the calculation of high-resolution convection models with 3-D spherical geometry is still time consuming, and a full reconstruction of the thermal evolution accounting for time variation in the Rayleigh number and uncertainties in the mantle properties would require an excessive computational time in 3-D spherical geometry. Note that calculations in 2-D spherical annulus (Hernlund & Tackley, 2008) are a promising alternative to model the evolution of planetary mantle, since they require much less computational resources than 3-D spherical calculations and predict heat transfer that compare well with those observed in 3-D spherical geometry. A more general method that has been extensively used to reconstruct the thermal evolution of planetary mantles is parametrized convection (e.g. for early studies, Sharpe & Peltier, 1978; Schubert *et al.* 1979; Davies, 1980; Stevenson *et al.* 1983). This method is based on the mantle energy balance and the use of scaling relationships for various observables (including the surface heat flux), and it uses simple

© 2010 The Authors
Journal compilation © 2010 RAS

and time sparing numerical methods. In the case of the Earth, however, plate tectonics may trigger changes of mantle flow patterns in time, and simple scaling laws fail to describe the mantle's thermal evolution (Labrosse & Jaupart, 2007). Despite this limitation, parametrized convection remains a good strategy to describe planetary mantle evolution to the first order. Furthermore, scaling laws provide a more general framework that can be applied to various planets (including hypothetical super-Earths) or moons rather than to one specific body, and that is essential to better understand the influence of individual parameters.

Thermal boundary layer (TBL) analysis provides a theoretical background to scaling laws, which are often considered as empirical relationships. This analysis is based on the balance between the convective and conductive heat flux at the boundary between the TBL and the bulk of the fluid. Cold descending slabs and hot rising plumes are generated from local instabilities in the top and bottom TBL, respectively. For an isoviscous fluid in Cartesian geometry, TBL analysis predicts that the heat flux scales as the Rayleigh number to the power 1/3 (Moore & Weiss, 1973; Turcotte & Schubert, 1982). This prediction has been extensively verified by numerical studies (e.g. Jarvis & Peltier, 1982; Christensen, 1984; Schubert & Anderson, 1985), but with a Rayleigh exponent b slightly smaller than 1/3 (most studies have found values of b between 0.31 and 0.32). Similar analyses were used for other setups, in particular for a mixed heated fluid in 3-D Cartesian geometry (Sotin & Labrosse, 1999; Choblet & Parmentier, 2009), and for a strongly temperature-dependent viscosity fluid in 2-D Cartesian geometry (Deschamps & Sotin, 2000). It should be noted, however, that the TBL analysis was developed asymptotically at very high Rayleigh number. Labrosse (2002), and more recently Moore (2008), argued that for a system with small ($<10^9$) Rayleigh number, the cold sinking slabs play a significant role in the growth of instabilities in the bottom TBL.

Planetary mantles are spherical shells, and it is important to understand the influence of spherical geometry on the heat flux scaling laws. Vangelov & Jarvis (1994) and Jarvis *et al.* (1995) performed calculations in axisymetric spherical shells with various curvatures. Using a TBL analysis, they showed that at any curvature the Nusselt number in spherical geometry can be deduced from the Nusselt number in Cartesian geometry, provided that the aspect ratio of the flow (defined as the ratio of the distance between neighbouring plumes at mid-depth to the shell thickness) is similar in both geometries. Ratcliff *et al.* (1996) conducted experiments in a spherical shell with Earth's mantle curvature for tetrahedral and cubic flow patterns, and for both isoviscous and slightly temperature-dependent viscosity fluids. They found that the Nusselt number slightly depends on the pattern, and proposed that the Nusselt number scales as the ratio between the Rayleigh number of the fluid layer and the Rayleigh number for the onset of convection. Iwase & Honda (1998) found that for a spherical shell with a curvature similar to that of the Earth's mantle the Rayleigh number exponent of the Nusselt number scaling law is similar to that in Cartesian geometry. Still in the case of a spherical shell with Earth's mantle curvature, Reese *et al.* (1999, 2005) derived heat flux scaling in the case of stagnant lid convection (i.e. for a fluid with large thermal viscosity ratios), and found only small differences compared to the Cartesian case. More recently, Shahnas *et al.* (2008) and Wolstencroft *et al.* (2009) proposed scalings for mixed and basal heating, respectively.

In this paper, we calculated models of isoviscous thermal convection for both basal and mixed heating in spherical geometry, from which we derive scaling laws that explicitly account for the spherical shell curvature.

2 NUMERICAL MODELLING

The numerical experiments reported in this study were performed with STAGYY (Tackley, 2008), a spherical version of STAG3D (Tackley, 1998). We solved the conservation equations of mass, momentum, and energy for an incompressible, isoviscous, infinite Prandtl number fluid in a spherical shell modelled by a yin-yang grid. At each depth, the yin-yang grid consists of two strips of equal size, which are combined like the two patches of tennis ball to generate a spherical surface (Kageyama & Sato, 2004). The strips' geometry induces small overlaps at the strips boundaries. STAGYY uses the minimum overlap defined by Kageyama & Sato (2004), in which the cells located at the corners of one strip, which are entirely contained within the other strip, are deleted. Each strip is used to calculate the boundary conditions for the other strip. In our calculations, the strips have a resolution of either 384×128 or 192×64 points. The vertical resolution is 64 points, and the grid is refined at the top and at the bottom of the shell to model TBLs more accurately. The shell thickness D is taken as unit length, and the ratio f of the core radius to the total radius of the sphere can be written

$$f = \frac{R_c}{R_c + D} = \frac{r_c}{1 + r_c}, \tag{1}$$

where R_c and r_c are the dimensional and non-dimensional core radius, respectively. The curvature of the convecting spherical shell is thus inversely proportional to f. As $r_c \to \infty$, $f \to 1$, that is, the geometry of the system tends to 3-D Cartesian. The second important parameter in our experiments is the Rayleigh number, which measures the vigour of convection and is defined by

$$Ra = \frac{\alpha \rho g \Delta T D^3}{\eta \kappa}, \tag{2}$$

where α, ρ, η and κ are the fluid thermal expansion, density, viscosity and thermal diffusivity, g is the gravitational acceleration and ΔT is the superadiabatic temperature difference between the bottom and the top of the shell. Scalar and vectorial quantities are calculated at the centre and on the side of each cell, respectively. The surface and core–mantle boundaries are free slip and isothermal. We considered two modes of heating. In one series of experiments, the fluid is heated from below and cooled from the top. In a second series, the fluid is heated both from below and from within, and cooled from the top. In the latter case, an additional input parameter is the non-dimensional rate of internal heating,

$$h = \frac{\rho H D^2}{k \Delta T}, \tag{3}$$

where H is the internal heating rate per unit mass, and k the thermal conductivity. At each time step, the conservation equations are solved using a Jacobi relaxation method. To speed up the convergence of the momentum and pressure equation, we used a multigrid algorithm (e.g. Stüben & Trottenberg, 1982). Time stepping (in the conservation of energy) is achieved by an explicit MPDATA (Smolarkiewicz, 1984) algorithm for advective terms, and a second-order finite difference scheme for diffusive terms. The initial condition for the temperature consists of 3-D-random perturbations, and the calculations are carried on until a stationary or quasi-stationary state is reached. For quasi-stationary cases, we averaged the temperature and heat flux over a time interval covering a significant number of the average temperature oscillations.

3 THERMAL BOUNDARY LAYER ANALYSIS

Heat transfer through a convective system is controlled by the properties of the TBLs that develop in this system. TBLs transfer heat by conduction, and the limit between a TBL and the bulk of the convective system may be defined as the place where the radial conductive and advective heat transfers are balancing. Using this definition, and noting that for an infinite Prandtl number the viscous and buoyancy forces are balancing everywhere in the system, the non-dimensional heat flux across a TBL, $Q_{\rm adim}$, scales as (e.g. Moore & Weiss, 1973; Sotin & Labrosse, 1999)

$$Q_{\rm adim} \propto Ra^{1/3} \left(\frac{\delta T}{\Delta T}\right)^{4/3}, \tag{4}$$

where δT is the temperature difference across the TBL. Following Howard (1966), the proportionality constant in eq. (4) is sometimes expressed in terms of a TBL Rayleigh number, Ra_δ,

$$Q_{\rm adim} = \left(\frac{Ra}{Ra_\delta}\right)^{1/3} \left(\frac{\delta T}{\Delta T}\right)^{4/3}, \tag{5}$$

$$\text{where} \quad Ra_\delta = \frac{\alpha \rho g \delta T d^3}{\eta \kappa} = \left(\frac{\delta T}{\Delta T}\right)\left(\frac{d}{D}\right)^3 Ra, \tag{6}$$

and d is the thickness of the TBL. Ra_δ can be understood as a measure of the TBL stability. The larger its value, the more difficult it is for instabilities to be generated and grow. In the asymptotic limit, Ra_δ is a constant, but 2-D and 3-D numerical studies pointed out that Ra_δ is a power law function of Ra,

$$Ra_\delta = a_0 Ra^\beta, \tag{7}$$

where the values of a_0 and β depend on the properties of the system, and in particular on the applied boundary conditions. Inserting eq. (7) into eq. (5), one gets

$$Q_{\rm adim} = a Ra^b \left(\frac{\delta T}{\Delta T}\right)^{(1+b)}, \tag{8}$$

where $Q_{\rm adim}$ is the non-dimensional heat flux, $a = a_0^{-1/3} (\delta T/\Delta T)^\beta$ and $b = (1-\beta)/3$.

In a system that is cooled on top and (at least partially) heated from below, two TBLs are present, and eq. (8) leads to expressions for the non-dimensional heat flux across the top and bottom TBLs (hereafter called top and bottom Nusselt numbers, $Nu_{\rm top}$ and $Nu_{\rm bot}$),

$$Nu_{\rm top} = a_{\rm top} Ra^{b_{\rm top}} \theta_m^{(1+b_{\rm top})} \tag{9a}$$

$$\text{and} \quad Nu_{\rm bot} = a_{\rm bot} Ra^{b_{\rm bot}} (1-\theta_m)^{(1+b_{\rm bot})}, \tag{9b}$$

where θ_m is the non-dimensional average temperature of the system. For a classical Rayleigh–Bénard system—Cartesian geometry, isoviscous fluid, basal heating only, similar surface and bottom mechanical boundary conditions—the top and bottom thermal boundary are symmetric, that is, that θ_m is equal to 0.5, $a_{\rm top} = a_{\rm bot}$ and $b_{top} = b_{\rm bot}$. Following eq. (6), the Rayleigh number of the top and bottom TBL are equal, that is, that the abilities of the top and bottom TBL to develop instabilities are similar. Additional complexities, including spherical geometry, internal heating, and variations of the fluid properties (viscosity, thermal expansion and thermal diffusivity) with temperature and/or depth, break this symmetry, and θ_m is no longer equal to 0.5.

In spherical geometry, symmetry between the top and bottom TBL is simply broken by the fact that their lateral extents are different. Conservation of energy requires that the top and bottom power are equal, which implies that heat flux is larger at the bottom of the shell than at its top. If there is no internal heating, the conservation of energy is thus written

$$\frac{Nu_{\rm top}}{Nu_{\rm bot}} = f^2. \tag{10}$$

Assuming that the conditions $a_{\rm top} = a_{\rm bot}$, and $b_{\rm top} = b_{\rm bot}$ are still valid, that is, that the Rayleigh number of the top and bottom TBL are equal, and that $\beta = 0$ (i.e. $(1+b) = 4/3$) as predicted by TBL analysis, one gets an expression for the average non-dimensional temperature as a function of f (Vangelov & Jarvis, 1994; Sotin & Labrosse, 1999):

$$\theta_m = \frac{f^{3/2}}{1+f^{3/2}}. \tag{11}$$

The presence of internal heating, in addition to the basal heating, modifies the relative strength of the TBLs (i.e. their ability to develop instabilities). The strength of the bottom TBL decreases as the amount of internal heating increases, that is, ascending plumes are less vigorous and the heat transfer is less efficient (e.g. McKenzie *et al.* 1974; Travis & Olson, 1994; Sotin & Labrosse, 1999; McNamara & Zhong, 2005). The conservation of energy must account for the internal source of heating, and the non-dimensional top and bottom heat flux, $Nu_{\rm top}$ and $Nu_{\rm bot}$, now follow:

$$Nu_{\rm top} = f^2 Nu_{\rm bot} + \frac{\left(1+f+f^2\right)}{3} h. \tag{12}$$

Sotin and Labrosse (1999) pointed out that TBL analysis cannot be applied to the bottom TBL, but is still valid to describe the top one. They suggest that in 3-D Cartesian geometry the average non-dimensional temperature is the sum of the temperatures for bottom and internal heating, and scales as

$$\theta_H = 0.5 + C \frac{h^{3/4}}{Ra^{1/4}}. \tag{13}$$

They found that $C = 1.236$ fit well their numerical experiments. By analogy with eq. (13), Sotin & Labrosse (1999) propose a scaling for spherical geometry

$$\theta_H = \frac{f^{3/2}}{1+f^{3/2}} + C(f) \left(\frac{1+f+f^2}{3}\right)^{3/4} \frac{h^{3/4}}{Ra^{1/4}}, \tag{14}$$

where $C(f)$ is a coefficient that depends on f only and is equal to 1.236 for $f = 1$. Note that the f polynomial in the expression of the temperature for internal heating results from the conservation of energy.

It should be noted that TBL analysis is an asymptotic theory and that heat transfer is dominated by TBL instabilities for high enough Rayleigh number only. The calculations of Lenardic & Moresi (2003) showed the TBL regime is valid for Rayleigh number of at least 10^9. For the range of Rayleigh numbers usually considered in planetary mantles studies (10^4–10^8), Labrosse (2002) and Moore (2008) suggested that the interaction between the sinking slabs and the bottom TBL plays a significant role in the heat transfer. Using 2-D and 3-D Cartesian calculations with free-slip boundaries and mixed heating, Choblet & Parmentier (2009) showed that the hot plumes rising from the bottom TBL modify the vertical velocity structure close by the top TBL, which in the case pure basal heating results in a 20–30 per cent decrease in the temperature difference across the top TBL compared to the scaling expected for a pure volumetric heating. This is consistent with eq. (7), which introduces a

slight departure from the TBL analysis and imposes the Rayleigh exponent of the heat flux scaling to be slightly lower than 1/3 (typically by 0.01 in the case of isoviscous, bottom heated convection). The heat transfer through the fluid layer is less efficient than predicted by the asymptotic TBL theory, which may be explained by the fact that the arrival of cold slabs (hot plumes) at the bottom (top) of the fluid slightly reduces the amount of heat that can be injected in (extracted from) the system. From that point of view, eq. (7) quantifies the interaction between plumes (or slabs) and TBLs.

4 BOTTOM HEATED FLUID

We conducted a total of 60 numerical experiments with bottom heating and the setup described in Section 2, varying the ratio f of the core to total radii between 0.3 and 0.8, and the Rayleigh number between 10^4 and 10^7 (Table 1). Figs 1 and 2 plot temperature isosurfaces and slices for various Rayleigh numbers and various f, and give qualitative information about the influence of each of these two parameters. With increasing Ra, the vigour of convection increases, and for a fixed value of f, the number of plume increases and the plumes becomes thinner (Fig. 1). With increasing f (decreasing curvature) the surface area of the bottom boundary increases, which allows the formation of a larger number of hot plumes (Fig. 2). For $f = 0.4$, thermal plumes have a spherical harmonics degree 1 distribution, that is, one plume only is generated (Figs 2a and b). For $f = 0.8$, on the contrary, we observe 10 plumes with an irregular distribution (Figs 2e and f). These results are consistent with linear stability analysis for a spherical shell (Chandrasekhar, 1961; Zebib *et al.* 1983) and numerical experiments in spherical geometry (Schubert *et al.* 1990; Behounkova & Choblet, 2009), which suggests that due to the increase in aspect ratio, the wavelength of the preferentially generated structures decreases with increasing f. Temperature profiles in Fig. 3(a) indicate that the average temperature decreases with decreasing f (increasing curvature), as previously pointed out by Jarvis *et al.* (1995) for an isoviscous fluid, and more recently for a temperature-dependent viscosity fluid (Behounkova & Choblet, 2009). This is related to the fact that the power available at the base of the shell is decreasing with decreasing f. To obtain more quantitative information that can be used to study the thermal evolution of a planetary mantle, it is essential to derive scaling laws for the temperature and the heat flux.

4.1 Temperature

A close examination at the average temperatures listed in Table 1 shows that our experiments do not follow eq. (11) (compare, for instance, the calculated temperatures at $f = 0.4$, 0.6 and 0.8 with the expected ones, 0.202, 0.317 and 0.417, respectively). Our values are smaller than those predicted by eq. (11) by 20 per cent on average, and the difference decreases as f increases, which is consistent with the fact that geometry tends towards 3-D Cartesian as f converges to 1. The increasing disagreement with decreasing f may be explained by the fact that the flow pattern converges to a spherical harmonics degree 1 distribution as f goes to zero (Jarvis *et al.* 1995). Shahnas *et al.* (2008) have also reported departure from eq. (11), and noted that their data are better explained by

$$\theta_m = \frac{f^2}{1 + f^{3/2}}. \qquad (15)$$

Table 1. Bottom heating: average temperature and surface Nusselt number.

f	Ra	Resolution	θ_m	$Nu_{\rm top}$
0.30	10^4	192×64×64×2	0.089	0.843
–	3.2×10^4	192×64×64×2	0.073	1.142
0.35	10^4	192×64×64×2	0.109	1.062
0.40	10^4	192×64×64×2	0.132	1.292
–	10^5	192×64×64×2	0.145	2.354
–	2.1×10^5	192×64×64×2	0.140	2.946
–	4.6×10^5	192×64×64×2	0.134	3.748
–	10^6	192×64×64×2	0.122	4.713
–	2.0×10^6	384×128×64×2	0.138	6.181
–	4.7×10^6	384×128×64×2	0.135	8.021
–	10^7	384×128×64×2	0.132	10.098
0.45	10^4	384×128×64×2	0.184	1.467
–	10^5	192×64×64×2	0.172	2.913
–	10^6	384×128×64×2	0.178	6.090
0.48	10^6	384×128×64×2	0.185	6.470
0.50	10^4	192×64×64×2	0.212	1.851
–	3.2×10^4	192×64×64×2	0.205	2.494
–	10^5	192×64×64×2	0.199	3.447
–	3.2×10^5	192×64×64×2	0.200	5.028
–	10^6	384×128×64×2	0.189	7.153
0.54	4.7×10^5	384×128×64×2	0.220	6.273
–	10^6	384×128×64×2	0.215	8.127
–	2.0×10^6	384×128×64×2	0.213	9.799
–	4.7×10^6	384×128×64×2	0.210	12.749
–	10^7	384×128×64×2	0.211	16.086
0.55	10^4	192×64×64×2	0.222	2.128
–	2.1×10^4	192×64×64×2	0.237	2.564
–	4.6×10^4	192×64×64×2	0.235	3.162
–	10^5	192×64×64×2	0.235	4.071
–	2.1×10^5	192×64×64×2	0.222	5.141
–	10^6	384×128×64×2	0.218	8.281
0.60	10^4	192×64×64×2	0.265	2.414
–	10^5	192×64×64×2	0.266	4.689
–	10^6	384×128×64×2	0.259	9.491
0.65	10^4	192×64×64×2	0.299	2.713
–	10^5	384×128×64×2	0.299	5.102
–	10^6	384×128×64×2	0.289	10.850
0.70	10^4	192×64×64×2	0.322	2.992
–	2.1×10^4	192×64×64×2	0.313	3.602
–	4.6×10^4	192×64×64×2	0.329	4.625
–	10^5	192×64×64×2	0.312	5.834
–	2.1×10^5	192×64×64×2	0.315	7.442
–	10^6	384×128×64×2	0.326	12.150
0.74	10^4	384×128×64×2	0.356	3.111
–	2.1×10^4	384×128×64×2	0.352	3.993
–	4.6×10^4	384×128×64×2	0.348	5.006
–	10^5	384×128×64×2	0.352	6.334
–	4.6×10^5	384×128×64×2	0.348	10.421
–	10^6	384×128×64×2	0.356	13.688
0.75	10^4	192×64×64×2	0.357	3.298
–	10^5	384×128×64×2	0.360	6.465
–	10^6	384×128×64×2	0.358	13.64
0.80	10^4	192×64×64×2	0.388	3.587
–	3.2×10^4	192×64×64×2	0.376	4.892
–	10^5	384×128×64×2	0.383	7.024
–	3.2×10^5	192×64×64×2	0.377	10.379
–	10^6	384×128×64×2	0.384	15.178
–	2.0×10^6	384×128×64×2	0.382	18.491
–	4.7×10^6	384×128×64×2	0.380	24.139
–	10^7	384×128×64×2	0.379	30.551

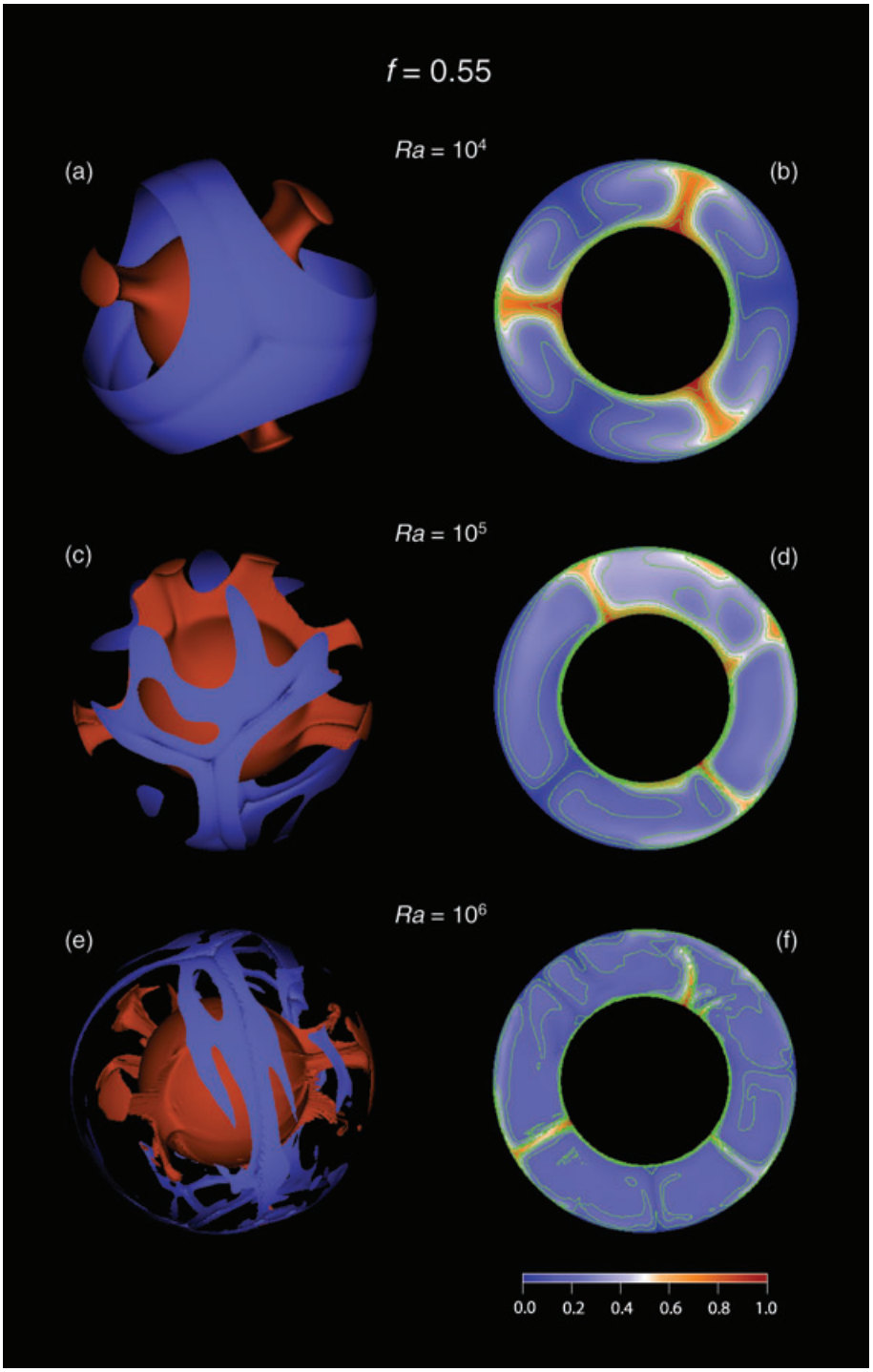

Figure 1. Effect of the Rayleigh number. The curvature is $f = 0.55$ ($r_c = 1.222$), and the Rayleigh number is equal to 10^4 (top row), 10^5 (middle row), and 10^6 (bottom row). The left column shows isosurfaces of the non-dimensional temperature. From top to bottom, the blue and red contour levels are $T = 0.005$, 0.0075 and 0.015, and $T = 0.55$, 0.55 and 0.50, respectively. The right-hand column shows slices of the non-dimensional temperature (scale indicated below). The green contours levels on the slices are from 0.0 to 1.0 with interval of 0.1.

eqs (11) and (15) are two particular cases of a more general family of functions of f,

$$\theta_m = \frac{\alpha f^{\beta_1}}{1 + (2\alpha - 1)\, f^{\beta_2}}, \tag{16}$$

which satisfy the boundary conditions on temperature ($\theta_m \rightarrow 0.5$ for $f \rightarrow 1$ and $\theta_m \rightarrow 0$ for $f \rightarrow 0$). To determine the values of α, β_1 and β_2, we inverted the temperature listed in Table 1 according to eq. (16), using a generalized non-linear inversion method (Tarantola & Valette, 1982), and an *a posteriori* analysis (Sotin, 1986; Appendix A) including the calculation of a χ^2 (eq. A4) to check the validity of the inversion. This approach has previously been used to infer scaling relationships for temperature and Nusselt number (Sotin & Labrosse, 1999; Deschamps & Sotin, 2000). Note that

© 2010 The Authors, *GJI*, **182,** 137–154
Journal compilation © 2010 RAS

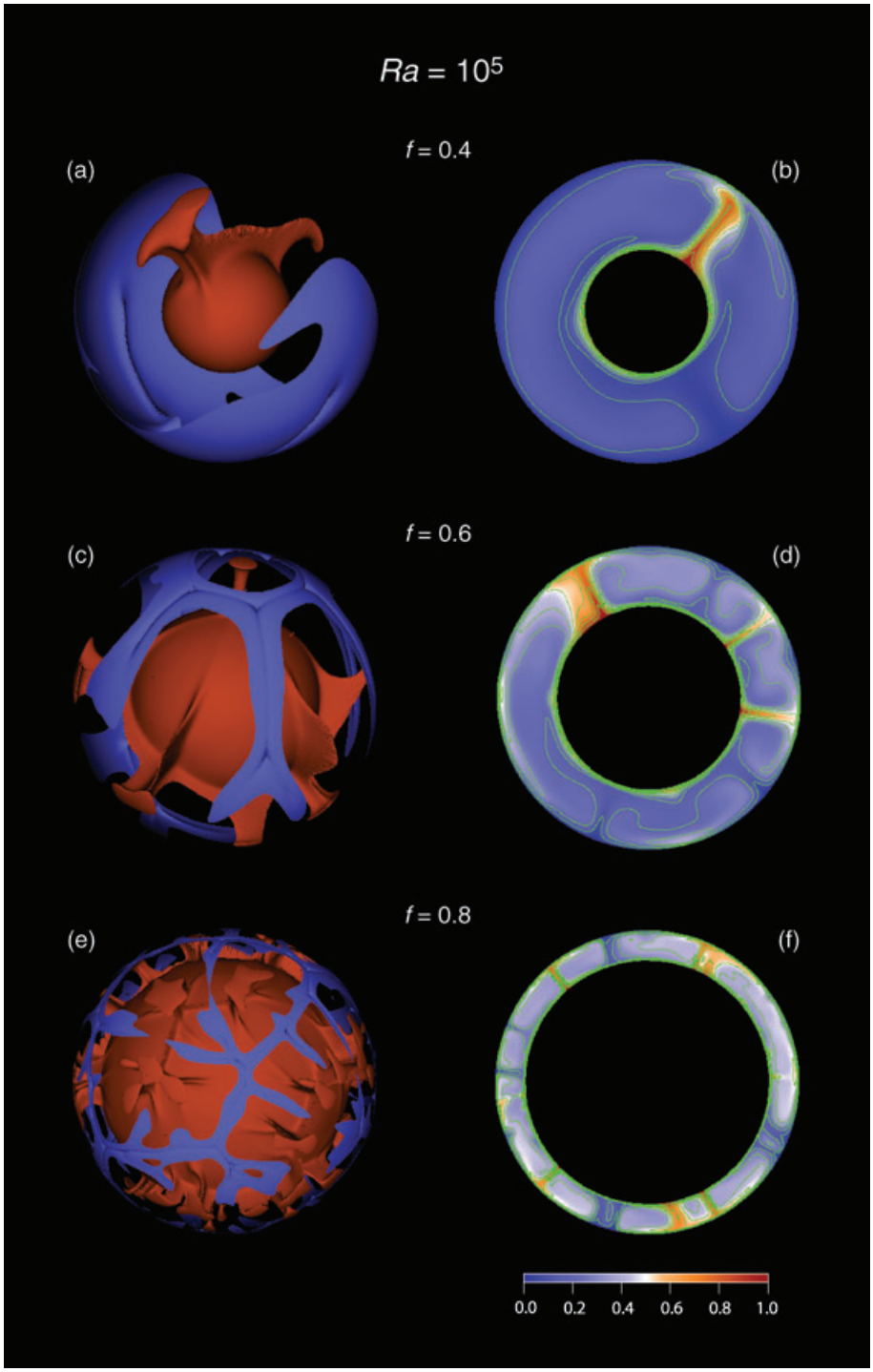

Figure 2. Effect of the curvature. The Rayleigh number is $Ra = 10^5$, and the curvature is equal to 0.4 ($r_c = 0.667$, top row), 0.6 ($r_c = 1.5$, middle row), and 0.8 ($r_c = 4.0$, bottom row). The left column shows isosurfaces of the non-dimensional temperature. From top to bottom, the blue and red contour levels are $T = 0.005$, 0.010 and 0.017, and $T = 0.55$, 0.55 and 0.60, respectively. The right-hand column shows slices of the non-dimensional temperature (scale indicated below). The green contours levels on the slices are from 0.0 to 1.0 with interval of 0.1.

given uncertainties in the observables, the non-linear generalized inversion provides uncertainties in the parameters. Inversion indicates that our data are best explained for $\alpha = 1.0 \pm 0.2$, $\beta_1 = 2.0 \pm 0.12$ and $\beta_2 = 2.0 \pm 0.10$, that is,

$$\theta_m = \frac{f^2}{1 + f^2}. \tag{17}$$

Fig. 4 compares the observed (red circles) and modelled (dashed black curve) values of θ_m. Modelled and observed temperatures differ by 1.6 per cent on average. Errors in the modelled θ_m were calculated from the *a posteriori* errors in the parameters (Table 3), and are represented by the grey dashed area in Fig. 4. Note that the expression proposed by Shahnas *et al.* (2008) (eq. 15, blue curve in Fig. 4) and the calculations of Jarvis *et al.* (1995) (green squares)

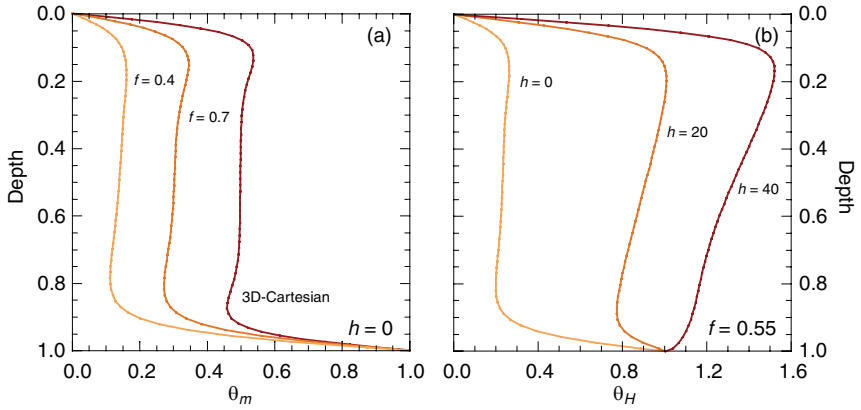

Figure 3. Temperature profiles for selected cases. Profiles are averaged out over a few time steps to account for small variations around the quasi-stationary state. (a) Influence of curvature. All profiles are for $Ra = 10^5$ and bottom heating, and three geometry are plotted: 3-D Cartesian, $f = 0.7$ ($r_c = 2.333$) and $f = 0.4$ ($r_c = 0.667$). (b) Influence of the amount of internal heating. All profiles are for $Ra = 10^5$ and $f = 0.55$ ($r_c = 1.222$), and three values of the non-dimensional rate of internal heating are plotted: $h = 0$, 20 and 40.

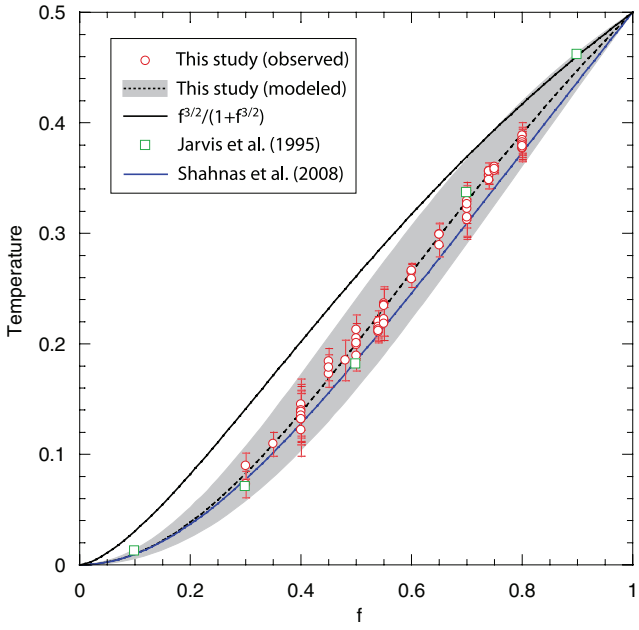

Figure 4. Observed (red dots) and modelled (dashed black curve and grey shaded area) internal temperature in the bottom heating case. The grey shaded area covers one error bar around the inverted scaling relationship (eq. 17), and error bars were calculated from *a posteriori* errors in the inverted paramaters (Table 3). For comparison, the green squares plot the calculations of Jarvis *et al.* (1995), and the plain black and blue curves show the temperature predicted by TBL analysis (Sotin & Labrosse, 1999) and by the calculations of Shahnas *et al.* (2008), respectively.

fall within our error bars, but that eq. (11) (thick black curve) does not.

Assuming that the temperature drops in the top and bottom TBLs are given by θ_m and $(1 - \theta_m)$, respectively, and combining eqs. (5), (10) and (17), the ratio between the Rayleigh numbers of the top and bottom TBLs can be written

$$\frac{Ra_{\delta,\mathrm{top}}}{Ra_{\delta,\mathrm{bot}}} = f^2. \tag{18}$$

If one understands the TBL Rayleigh number as a critical value for instabilities to grow in the TBL, eq. (18) indicates that hot instabilities (rising from the bottom TBL) are more difficult to generate than cold instabilities (sinking from the top TBL), and that this discrepancy increases with increasing curvature (decreasing f). An alternative interpretation considers the TBL Rayleigh numbers as local Rayleigh numbers. According to this view, eq. (18) leads to the opposite conclusion, that is, the bottom TBL is more active than the top one.

4.2 Heat flux

For a bottom heated fluid, the input and output powers are equal, and spherical geometry implies that the heat flux is larger at the bottom of the shell than at its top. The non-dimensional top and bottom heat flux, Nu_{top} and Nu_{bot}, hereafter called surface and bottom Nusselt numbers, are related by eq. (10). In addition, for comparison with previous studies (Jarvis *et al.* 1995; Ratcliff *et al.* 1996; Shahnas *et al.* 2008), it is convenient to define the Nusselt number by

$$Nu = \frac{Nu_{\mathrm{top}}}{f} = f Nu_{\mathrm{bot}}, \tag{19}$$

which is equivalent to spread the power transported by convection on a sphere of radius $r = \sqrt{r_c(1 + r_c)}$. In this study, we independently calculated the top and bottom Nusselt numbers, Nu_{top} and Nu_{bot}, checked that they verify the energy conservation (eq. (10)), and inverted our Nu_{top} values (Table 1) for an appropriate scaling law. Scaling relationships for Nu_{bot} and Nu can be deduced from the Nu_{top} scaling and from eqs (10) and (19), respectively.

The relationship we inferred for temperature (eq. 17) suggests that the parameters in eq. (9) may explicitly depend of the curvature (note that eq. 9 implicitly depend on curvature through the temperature, θ_{m}), and that they may be different for the top and bottom TBL. It is not unreasonable to assume that the pre-exponential factor, a, is different for the top and bottom TBL and may depend on f. On the contrary, different values of the Rayleigh number exponent, b, for the top and bottom TBL would make it difficult to satisfy the conservation of energy (eq. 10), which our experiments obey very well. Our experiments suggest that b is indeed similar for the top and bottom Nusselt number, but that it slightly depends on f. Finally, one may consider the possibility that the internal temperature exponent, c, is not equal to $(1 + b)$. Following these remarks, eq. (9a) can be rewritten

$$Nu_{\mathrm{top}} = a_1 f^{a_2} Ra^{(b_1 + b_2 f)} \theta_m^c. \tag{20}$$

© 2010 The Authors, *GJI*, **182,** 137–154
Journal compilation © 2010 RAS

Assuming that θ_m is given by eq. (17), we have inverted our observed Nu_{top} (Table 1) for the five parameters in eq. (20), and found that c strongly trades off with a_2 and, to a lesser extent, with a_1. This result is not surprising given eq. (17). A more straightforward expression for Nu_{top} would be to write the product $a = a_1 f^{a_2} \theta_m^c$ as the ratio of two polynomials of f. eq. (20) has however the advantage to explicitly relate the surface Nusselt number to the internal temperature. The minimum χ^2 is obtained for $a_1 = 0.36 \pm 0.04$, $a_2 = 0.32 \pm 0.4$, $b_1 = 0.273 \pm 0.007$, $b_2 = 0.05 \pm 0.01$ and $c = 0.6 \pm 0.2$, but other solutions with slightly larger χ^2 also explain our calculations well within error bars. A specific solution may be chosen by fixing a range of values for c, provided that the χ^2 remains reasonable (i.e. comparable to the number of experiments, 60 in our case) within this range. For instance, when fixing the temperature exponent to $c = 4/3 \pm 0.1$, as suggested by TBL analysis, we found that $a_1 = 0.50 \pm 0.05$, $a_2 = -1.0 \pm 0.2$, $b_1 = 0.257 \pm 0.007$ and $b_2 = 0.08 \pm 0.01$, with a good χ^2 (Table 3). Whatever the curvature, the two scalings we proposed differ from one another by less than 10 per cent for Rayleigh numbers in the range 10^3–10^9.

For comparison and presentation of the results it is convenient to define a reduced Nusselt number, in which the dependence on f has been balanced,

$$Nu_r = \frac{Nu_{top}}{f^{a_2} Ra^{b_2 f} \theta_m^c} = a_1 Ra^{b_1}. \quad (21)$$

The reduced Nusselt number is then a power law of the Rayleigh number. Fig. 5 compares our calculations (red dots) and the scaling obtained for the minimum χ^2 (dotted curve and shaded area). Modelled and observed Nusselt number differ by 4.0 per cent on average. Note that within error bars, our scaling for the surface heat flux also explains the results of Jarvis *et al.* (1995) (green squares), Ratcliff *et al.* (1996) (brown triangles) and Wolstencroft *et al.* (2009) (blue diamonds). Similarly, the scaling obtained by fixing c to 4/3 explains our calculations and those of Jarvis *et al.* (1995), Ratcliff *et al.* (1996) and Wolstencroft *et al.* (2009) very well. Note that our scaling law explains the calculations of Ratcliff *et al.* (1996), but differs from the scaling law proposed by these authors for $f = 0.55$. Part of the disagreement is due to the fact that Ratcliff *et al.* (1996) built their scaling laws using both isoviscous and slightly temperature-dependent viscosity (up to a ratio of 30) fluids. Most of the discrepancy, however, may result from the fact that we try to fit experiments with flow patterns having different aspect ratio to one single scaling law (see discussion in Section 7).

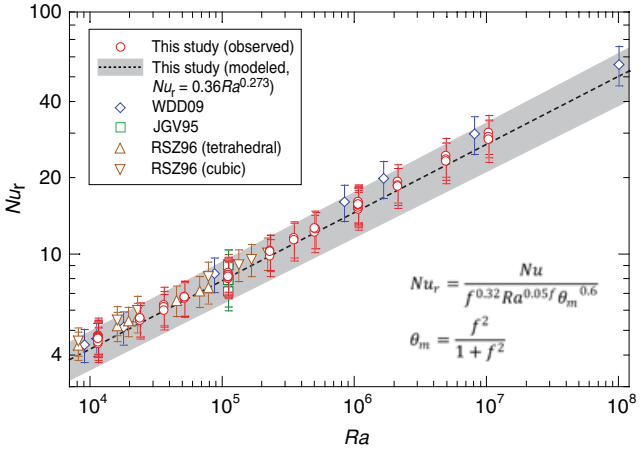

Figure 5. Reduced Nusselt (eq. 21) number as a function of Rayleigh number in the bottom heating case. The Nusselt number is calculated from eq. (20) and the minimum χ^2 values of the parameters (Table 3). Red dots represent our calculations, and the green squares, brown triangles and blue diamonds those of Jarvis *et al.* (1995), Ratcliff *et al.* (1996) and Wolstencroft *et al.* (2009), respectively. Note that the Nusselt number listed in these studies correspond to the definition of Nu in eq. (19), and must be multiplied by f for comparison with our Nu_{top}. The grey band covers one error bar around the value predicted by inversion (black dashed curve). Error bars were calculated from the *a posteriori* uncertainties in a_2, b_2 and c (Table 3), and assuming an *a priori* 3 per cent error on the calculated Nu_{top}.

Scalings for the bottom Nusselt number can be deduced from eqs (10) and (20). However, to validate our inversion procedure, it is important to directly invert our observed values of Nu_{bot} for an independent relationship. Following the same approach as for Nu_{top}, we assumed that the internal temperature θ_m is given by eq. (17), and that Nu_{bot} fits well along

$$Nu_{bot} = a_1 f^{a_2} Ra^{(b_1 + b_2 f)} (1 - \theta_m)^c. \quad (22)$$

Again, strong trade-offs exist between a_1, a_2 and c. The minimum χ^2 solution is $a_1 = 0.37 \pm 0.04$, $a_2 = -0.35 \pm 0.08$, $b_1 = 0.274 \pm 0.007$, $b_2 = 0.05 \pm 0.01$ and $c = 0.6 \pm 0.2$, which is fully consistent with eq. (10) and the minimum χ^2 solution found for Nu_{top}. In particular, note that the Rayleigh number and temperature exponents (b_1, b_2 and c) are unchanged. Fixing c to $4/3 \pm 0.1$, we found $a_1 = 0.50 \pm 0.05$, $a_2 = -0.33 \pm 0.09$, $b_1 = 0.257 \pm 0.007$ and $b_2 = 0.08 \pm 0.01$, with $\chi^2 = 52.6$. Again, this specific solution is consistent with eq. (10) the scaling found for Nu_{top} and $c = 4/3$.

5 MIXED HEATING

Mixed heating is better suited to model convection and heat transfer in planetary mantles. Sources of internal heating include the decay of radiogenic elements, the mantle's secular cooling (Krishnamurti, 1968; Daly, 1980; Choblet & Sotin, 2000), and tidal heating (e.g. Galilean moons). Calculations in various geometries showed that the flow pattern and heat transfer are very sensitive to the relative amount of bottom and internal heating (Travis & Olson, 1994; Sotin & Labrosse, 1999; McNamara & Zhong, 2005; Shahnas *et al.* 2008). Increasing the volumetric heating rate h reduces the strength of the bottom TBL. Hot plumes are less vigorous and, if h is large enough, they may not reach the surface (Labrosse, 2002). The heat transfer through the convective layer is less efficient than in the bottom heating case, and the average temperature of the bulk interior increases.

We performed 56 numerical experiments with mixed heating in spherical geometry, varying f, Ra and the non-dimensional rate of internal heating h (eq. (3)) (Table 2). Note that the grid size is $384 \times 128 \times 64 \times 2$ in all calculations. Fig. 6 plots temperature slices for a few cases. In agreement with previous studies, the average temperature increases as h increases, hot plumes are less vigorous, and the geotherm is sub-adiabatic over a thicker layer (Fig. 3b). For $h = 40$ and $Ra = 10^5$, the geotherm is subadiabatic throughout most of the shell thickness and the bottom TBL has disappeared, that is, the convective shell does not extract heat from the core. Following Sotin & Labrosse (1999), we assumed that the internal temperature θ_H can be explained by the sum of the temperature for bottom heating, θ_m, and a term that depends on h. In spherical geometry, this additional term also depends on the curvature, and the internal temperature can be written

$$\theta_H = \theta_m + (\alpha_1 + \alpha_2 f) \left(\frac{1 + f + f^2}{3} \right)^{\beta} \frac{h^{\beta}}{Ra^{\gamma}}. \quad (23)$$

Table 2. Mixed heating: average temperature and surface Nusselt number.

f	Ra	h	$\theta_{\rm H}$	$Nu_{\rm top}$
0.40	10^4	5.0	0.486	3.740
–	10^4	20.0	1.159	10.290
–	10^4	40.0	1.763	19.629
–	3.2×10^4	40.0	1.418	20.028
–	10^5	5.0	0.324	4.815
–	10^5	10.0	0.473	7.001
–	10^5	20.0	0.721	11.342
–	10^5	30.0	0.915	15.840
–	10^5	40.0	1.120	20.602
–	10^5	50.0	1.309	25.419
–	3.2×10^5	40.0	0.896	21.491
–	10^6	5.0	0.245	7.466
–	10^6	20.0	0.474	13.747
–	10^6	40.0	0.724	22.836
0.50	10^5	5.0	0.388	6.019
–	10^5	10.0	0.549	8.331
–	10^5	20.0	0.804	12.940
–	10^5	30.0	0.995	17.625
–	10^5	40.0	1.215	22.892
0.55	10^4	5.0	0.603	4.492
–	10^4	20.0	1.278	11.743
–	3.2×10^4	20.0	1.024	12.602
–	10^5	20.0	0.848	13.735
–	3.2×10^5	20.0	0.708	15.342
–	10^6	20.0	0.593	17.644
–	10^4	40.0	1.938	22.276
–	3.2×10^4	40.0	1.560	23.112
–	10^5	40.0	1.257	24.056
–	3.2×10^5	40.0	1.021	25.538
–	10^6	40.0	0.839	27.691
–	10^5	50.0	1.461	29.510
0.60	10^5	5.0	0.457	7.261
–	10^5	10.0	0.632	9.659
–	10^5	20.0	0.884	14.472
–	10^5	30.0	1.085	19.528
–	10^5	40.0	1.306	25.197
0.70	10^5	5.0	0.523	8.560
–	10^5	10.0	0.706	10.879
–	10^5	20.0	0.955	15.979
–	10^5	30.0	1.165	21.655
–	10^5	40.0	1.397	27.523
0.80	10^4	5.0	0.766	5.921
–	10^4	20.0	1.436	14.432
–	10^4	30.0	1.821	20.505
–	10^4	40.0	2.206	26.734
–	3.2×10^4	40.0	1.805	28.205
–	10^5	5.0	0.593	9.722
–	10^5	10.0	0.776	11.982
–	10^5	20.0	1.025	17.418
–	10^5	30.0	1.255	24.528
–	10^5	40.0	1.489	29.809
–	10^5	50.0	1.711	36.390
–	3.2×10^5	40.0	1.214	31.980
–	10^6	5.0	0.475	18.183
–	10^6	20.0	0.753	24.146
–	10^6	40.0	0.982	35.596

Grid size is $384 \times 128 \times 64 \times 2$ for all calculations

Shahnas *et al.* (2008) introduced a more complex expression for the coefficient C (eq. 14), assuming that it depends on the Rayleigh number. Here, we prefer to remain close to the expression predicted by TBL analysis (eq. 14), and assume that C is a linear function of f. Our inversion procedure treats the Rayleigh exponent γ as a free parameter, and thus insures that any dependence of C on the Rayleigh number will be accounted for. The choice to impose the same exponent β to the geometric factor $(1 + f + f^2)/3$ and to the internal heating rate h was dictated by the conservation of energy (eq. 12) at the limit of very high internal heating ($Nu_{\rm bot} = 0$). Assuming that θ_m is given by eq. (17), we have inverted the temperature in Table 2 for the parameters in eq. (23), and found that $\alpha_1 = 1.68 \pm 0.07$, $\alpha_2 = -0.8 \pm 0.04$, $\beta = 0.779 \pm 0.006$ and $\gamma = 0.234 \pm 0.003$. With these values, and within error bars, Eq. (23) explains well our calculations (red dots in Fig. 7) and those from Shahnas *et al.* (2008) (blue dots in Fig. 7). The relative difference between modelled and observed temperatures is 0.6 per cent on average, with a maximum of 2.0 per cent. Average and maximum discrepancies between our scaling and the results of Shahnas *et al.* (2008) are 0.8 and 2.8 per cent, respectively. In 3-D Cartesian geometry, the average temperature for isoviscous convection with mixed heating is well described by $\theta_H = 0.5 + 1.02h^{0.729}/Ra^{0.232}$ (Sotin & Labrosse, 1999). The value of C predicted by our scaling for $f = 1$ is slightly smaller than the value found by Sotin & Labrosse (1999) (0.87 ± 0.11 instead of 1.02), but this is compensated by a slightly larger exponent of the internal heating rate (0.779 ± 0.006 instead of 0.729). As a result, our scaling for $f = 1$ explains very well the 3-D Cartesian calculations of Sotin & Labrosse (1999) (green squares in Fig. 7). Sotin & Labrosse (1999) have also inverted their results following TBL analysis (the internal heating rate and Rayleigh number exponents are fixed to 3/4 and 1/4, respectively, eq. 13) and found $C = 1.236$. Again, our value of C for $f = 1$ is smaller, but is compensated by a slightly larger exponent of the internal heating rate and a slightly lower exponent of the Rayleigh number. Within error bars, our scaling for $f = 1$ is fully consistent with that predicted by TBL analysis in 3-D Cartesian geometry.

Using the same approach as in the bottom heating case, we have then inverted the surface Nusselt numbers in Table 2 according to

$$Nu_{\rm top} = a_1 f^{a_2} Ra^{(b_1 + b_2 f)} \theta_H^c, \tag{24}$$

where θ_H is given by eq. (23) and parameter values in Table 3. Again, strong trade-offs exist between the parameters in eq. (24). Unlike the bottom heating case, however, only a small range of values of c explain our calculations well, that is, with a reasonable χ^2. Parameter values are overall less well constrained than in the bottom heating case. The minimum χ^2 solution is obtained for $a_1 = 0.59 \pm 0.06$, $a_2 = 0.05 \pm 0.15$, $b_1 = 0.300 \pm 0.01$, $b_2 = -0.003 \pm 0.02$ and $c = 1.23 \pm 0.02$. Fixing c to $4/3 \pm 0.03$ leads to solutions with χ^2 between 65 and 100. Fig. 8 compares the observed (red dots) and modelled (dotted curve and grey shaded area) reduced surface Nusselt number. Because uncertainties in the inverted values of the parameters are large, we observe more dispersion than in the bottom heating case. The relative difference between modelled and observed Nusselt numbers is 2.0 per cent on average with a maximum of 16 per cent (note that this difference is still within the error bars of our scaling). Our scaling also explains the calculation of Shahnas *et al.* (2008) for $f = 0.547$ (blue diamonds; note that the Q_s in their Table 4 correspond to our $Nu = Nu_{\rm top}/f$).

The scaling laws we inferred for temperature (eq. 23) and the surface heat flux (eq. 24 with minimum χ^2 values of the inverted parameters) indicate that for a fixed value of h, both the average temperature and surface heat flux increase with f. The temperature decreases with increasing Rayleigh number, and this effect is amplified with increasing h. Also, note that the increase in surface heat flux with f strongly increases with Rayleigh number.

One may point out that the scaling laws we inferred for bottom and mixed heating are not continuous at $h = 0$. Sotin & Labrosse

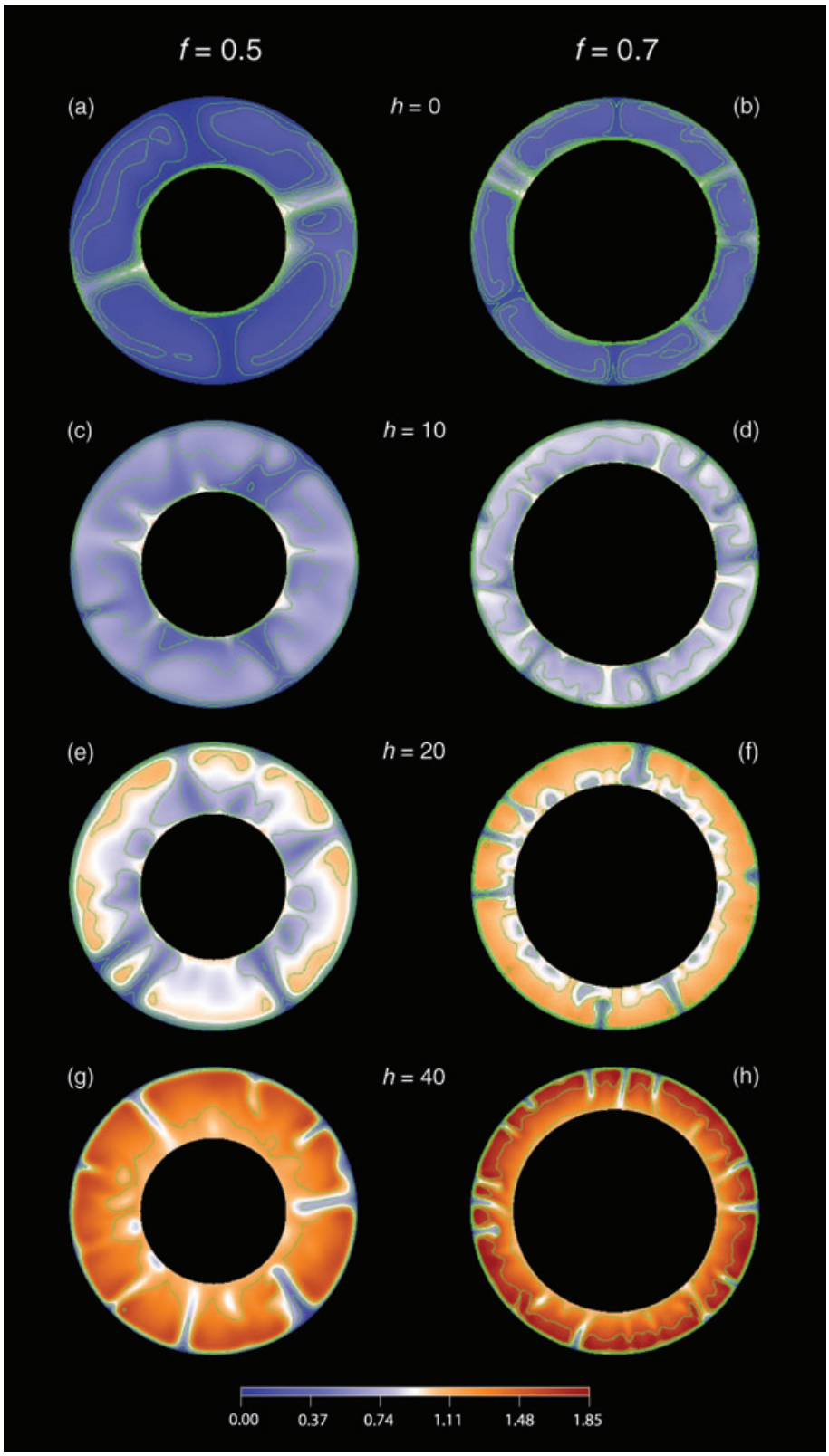

Figure 6. Effect of the rate of internal heating. Left and right columns show slices of the non-dimensional temperature (scale indicated below) for $f = 0.50$ ($r_c = 1.0$) and $f = 0.70$ ($r_c = 2.333$), respectively. The top row is for bottom heating only, and the middle and bottom rows for a non-dimensional rate of internal heating $h = 10$, 20 and 40, respectively. The green contours levels on the slices are start from 0.0 with interval of 0.1 (top row), 0.2 (middle rows) and 0.4 (bottom row).

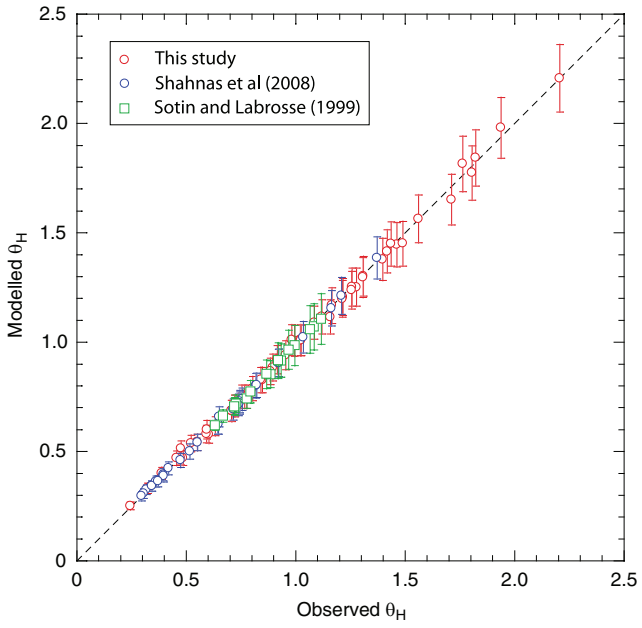

Figure 7. Comparison between observed and modelled average temperatures in the mixed heating case. Modelled temperatures are calculated from eq. (23) with parameters value listed in Table 3. Red and blue dots represent our calculations and those from Shahnas *et al.* (2008), respectively. Green squares show the 3-D Cartesian calculations of Sotin & Labrosse (1999). The error bars are calculated from the *a posteriori* uncertainties in the parameter values.

(1999) reported a similar disagreement in 3-D Cartesian geometry. Whatever the curvature and the Rayleigh number, the scaling obtained for mixed heating with $h = 0$ predicts a surface heat flux lower than that predicted by the scaling for bottom heating. To investigate further this disagreement, we performed a joint inversion of all the experiments for bottom heating Table 1) and mixed heating (Table 2) following eq. (24). The minimum χ^2 solution is obtained for $a_1 = 0.51 \pm 0.03$, $a_2 = -0.28 \pm 0.08$, $b_1 = 0.263 \pm 0.007$, $b_2 = 0.05 \pm 0.01$ and $c = 1.01 \pm 0.07$, but the minimum χ^2 is high, around 330. Thus, assuming that the surface heat flux is described by eq. (24), our experiments with bottom and mixed heating cannot be explained by a single scaling law. This suggests that convection undergoes two distinct regimes depending on whether volumetric heating is present or not, that is, the flow pattern and the mechanism that control the heat transfer are different. As the rate of volumetric heating increases, instabilities in the bottom TBL are weakening (if h is large enough, the bottom TBL even vanishes), and the heat transfer is mostly controlled by instabilities in the top TBL (Sotin & Labrosse, 1999).

6 INFLUENCE OF CURVATURE ON THE HEAT TRANSFER THROUGH PLANETARY MANTLES

Because they do not account for important physical complexities (see discussion in Section 7), our scaling laws may not be ideally suited to study the cooling of the Earth's mantle. However, they allow studying the influence of curvature on the cooling of planetary mantle, which we do in this section.

With eqs (20) and (24), we can estimate the heating power transported by convection as a function of the curvature and of the rate of internal heating. For bottom heating, Fig. 9(a) indicates that for a fixed value of the Rayleigh number, heat transfer becomes more efficient with increasing f. This is consistent with the observation that plumes are more easily generated with increasing f. In the case of mixed heating, it is convenient to define the convective Urey ratio between the volumetric heating, and the total surface power. For a planet of radius R_p and core radius R_c, the Urey ratio can be written

$$Ur = \frac{\frac{4\pi}{3}\left(R_p^3 - R_c^3\right) H \rho_m}{4\pi R_p^2 F_{surf}}, \tag{25}$$

where ρ_m the density of the mantle, $F_{\rm surf}$ is the surface convective heat flux and H is the internal heating rate per unit mass. Note that the convective Urey ratio (eq. (25)) differs from the observed Urey ratio, which is defined as the ratio between the radiogenic heating power and the total surface heat flow. The convective and observed Urey ratios are equal if the only source of internal heating is radiogenic heating, but they may significantly differ if the contribution of mantle secular cooling is important (i.e. if the mantle is not in a statistically steady state). Using the definition of the non-dimensional rate of internal heating (eq. 3), scaling the heat flux as $k\Delta T/D$ (where $D = R_p - R_c$ is the mantle thickness, and ΔT the superadiabatic temperature difference across the mantle), and noting that $f = R_c/R_p$, we obtain

$$Ur = \frac{h}{Nu_{\rm top}}\left(\frac{1 + f + f^2}{3}\right). \tag{26}$$

The Urey ratio measures the fraction of the surface power that originates from internal heating, and its complement to one ($1 - Ur$) measures the amount of energy that is extracted from the core and transferred to the surface. This amount decreases with increasing Urey ratio, and a Urey ratio larger than 1 indicates that convection is not able to cool down the core (the bottom heat flux is negative). Fig. 9(b) displays the Urey ratio (eq. 26) as a function of the Rayleigh number, and for $f = 0.55$ and several values of h. As expected, the Urey ratio increases with the rate of internal heating, that is, the fraction of heat that can be extracted from the core and transferred to the surface decreases with increasing h. More interestingly, for fixed values of h and Ra, the Urey ratio reaches a minimum for a value of f that increases with Ra (Fig. 9c) and decreases with h (not shown here). Thus, given the thickness of a spherical shell (i.e. the volume of the shell is only controlled by the radius of the core or equivalently, f), there is a ratio f_0 of core to total radii ratio for which the heat transfer through this shell is largest. This effect results from a competition between the total radiogenic power, which increases with increasing volume of the shell (thus, with increasing R_c and f), and the convective heat flow, which increases with f. Note that f_0 increases with Ra (because the convective heat flow increases with Ra) and decreases with increasing h (because the radiogenic power increases with h) (Fig. B1a). The values of f_0 and Ur_{min} as a function of Ra and h are calculated in Appendix B. If Ra is large enough (e.g. $> 10^7$ for $h = 20$, Fig. 9c), the convective heat flow remains dominant for all curvatures.

In the case of an isoviscous spherical shell with properties similar to that of the Earth's mantle ($f = 0.55$, $D = 2891$ km, $k = 5.6$ W m^{-1} K, $\Delta T = 2500$ K, and $\rho_m = 4500$ kg m^{-3}), thermal convection can extract heat from the core and transport it to the surface for non-dimensional rate of internal heating up to $h = 60$ for $Ra = 10^6$ and $h = 120$ for $Ra = 10^7$. Assuming that radiogenic heating is the only source of internal heating (i.e. the Earth's mantle is in steady state), these values of h correspond to radiogenic heating between $H = 1.63 \times 10^{-11}$ and 3.26×10^{-11} W kg^{-1}, that is, much larger than the estimated present-day value ($H = 6.0 \times 10^{-12}$ W kg^{-1}). Still neglecting the mantle secular cooling, the present-day value of

Table 3. Scaling laws for internal temperature and surface heat flux in spherical geometry.

Scaling	Inverted parameters	χ^{2a}
Bottom heating		
Average temperature (bottom heating)		
$\theta_m = \frac{\alpha f^{\beta_1}}{1+(2\alpha-1)f^{\beta_2}}$	$\alpha = 1.0 \pm 0.20$	55.4
	$\beta_1 = 2.0 \pm 0.12$	
	$\beta_2 = 2.0 \pm 0.10$	
Surface Nusselt number (minimum χ^2)		
$Nu = a_1 f^{a_2} Ra^{(b_1+fb_2)}\theta_m^c$	$a_1 = 0.360 \pm 0.040$	40.7
	$a_2 = 0.320 \pm 0.400$	
	$b_1 = 0.273 \pm 0.007$	
	$b_2 = 0.050 \pm 0.010$	
	$c = 0.600 \pm 0.200$	
Surface Nusselt number ($c = 1.33 \pm 0.1$)		
$Nu = a_1 f^{a_2} Ra^{(b_1+fb_2)}\theta_m^{4/3}$	$a_1 = 0.500 \pm 0.050$	51.0
	$a_2 = -1.000 \pm 0.200$	
	$b_1 = 0.257 \pm 0.007$	
	$b_2 = 0.080 \pm 0.010$	
Mixed heating		
Average temperature (mixed heating)		
$\theta_H = \theta_m + (\alpha_1 + \alpha_2 f)\left(\frac{1+f+f^2}{3}\right)^{\beta} \frac{h^\beta}{Ra^\gamma}$	$\alpha_1 = 1.680 \pm 0.070$	52.7
	$\alpha_2 = -0.800 \pm 0.040$	
	$\beta = 0.779 \pm 0.006$	
	$\gamma = 0.234 \pm 0.003$	
Surface Nusselt number (minimum χ^2)		
$Nu = a_1 f^{a_2} Ra^{(b_1+fb_2)}\theta_H^c$	$a_1 = 0.590 \pm 0.060$	50.4
	$a_2 = 0.050 \pm 0.150$	
	$b_1 = 0.300 \pm 0.010$	
	$b_2 = -0.003 \pm 0.020$	
	$c = 1.230 \pm 0.020$	
Surface Nusselt number ($c = 1.33 \pm 0.03$)		
$Nu = a_1 f^{a_2} Ra^{(b_1+fb_2)}\theta_H^{4/3}$	$a_1 = 0.520 \pm 0.080$	82.8
	$a_2 = 0.080 \pm 0.160$	
	$b_1 = 0.320 \pm 0.016$	
	$b_2 = -0.014 \pm 0.020$	

[a]The χ^2 is defined in Appendix A, eq. (A4).

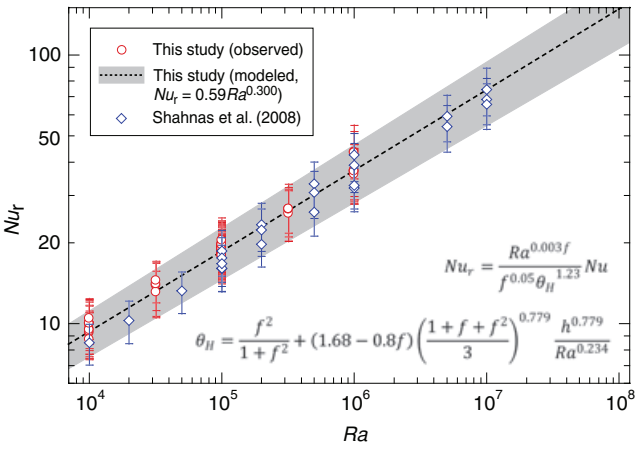

Figure 8. Reduced Nusselt number as a function of Rayleigh number in the mixed heating case. The Nusselt number is calculated from eq. (24) and the minimum χ^2 values of the inverted parameters (Table 3). Red dots represent our calculations, and the blue diamonds those of Shahnas *et al.* (2008). The grey band cover one error bar around the value predicted by inversion (black dashed curve). Error bars were calculated from the *a posteriori* uncertainties in a_2, b_2 and c (Table 3).

the non-dimensional rate of internal heating for the Earth mantle is about $h = 16$, which leads to a Urey ratio between 0.43 for $Ra = 10^7$ and 0.62 for $Ra = 10^6$. Table 4 lists numerical applications for other planets. Note that the uncertainty in the radius of Mars' core results in significant differences in the Urey ratio estimates. In this case, our calculations indicate that the cooling increases with increasing core radius.

Due to the formation of a stagnant lid at the top of the system, the efficiency of heat transfer is significantly reduced when large thermal viscosity ratios are present (e.g. Christensen, 1984; Moresi and Solomatov, 1995; Deschamps & Sotin, 2000). Thus, if convection in planetary mantles undergoes the stagnant lid regime, the Urey ratios listed in Table 4 are underestimated. Note that compared to the 'pure' stagnant lid regime, the heat transfer is slightly more efficient when depth-dependent viscosity is also included in the models (Dumoulin *et al.* 1999). In the case of the Earth, however, the stagnant lid regime is unrealistic because it would prevent plate tectonics.

The Earth's mantle Urey ratio predicted by our scaling is significantly larger than the observed one, which is currently estimated to be between 0.2 and 0.4 (Korenaga, 2008). First, it should be pointed out that our estimates are based on the convective Urey ratio (eq. (25)), which is equivalent to the observed Urey ratio if the Earth's mantle is in steady state, but overestimates it if the contribution of mantle secular cooling to internal heating is important. The

Table 4. Urey ratio estimates for various planets.

Planet[a]	R_c (km)	f	ΔT (K)	Ra	h	Urey[b]
Earth	3480	0.55	2500	10^6–10^7	16	0.43–0.62
Mercury	1800	0.74	1500[c]	2.0×10^4–2.0×10^5	1	0.11–0.19
Mars	1500	0.44	1750[d]	3.0×10^5–3.0×10^6	8	0.41–0.58
	1900	0.56	–	6.0×10^5–6.0×10^6	5	0.22–0.35

[a]Thermal expansion, diffusivity, and conductivity of Mars and Mercury are assumed similar to those of the Earth's Mantle. We assumed $\rho_m = 3800$ and 3500 kg m^{-3} for Mars and Mercury mantle density, respectively, and the reference bulk viscosity is assumed one order of magnitude smaller than for the Earth lower mantle. We considered two values for Mars' core radius corresponding to the current lower and upper estimates.
[b]Convective Urey ratio. The secular cooling is neglected, and the only source of internal heating is radiogenic heating with $H = 6.0 \times 10^{-12}$ W kg^{-1}.
[c]Extrapolated from the Martian geotherm of Khan & Connolly (2008).
[d]From Khan & Connolly (2008).

presence of reservoirs of dense material enriched in radiogenic elements is buried in the deep mantle (Kellogg *et al.* 1999) may further explain the disagreement between predicted and observed values. For instance, assuming that these reservoirs are enriched in radiogenic elements by a factor 10 and represent 10 per cent of the mantle in volume, the observed Urey ratio would rise by a factor 2. Another possible explanation is that due to changes in the aspect ratio of convection cells induced by change in the plate tectonic regime, the mantle heat flux strongly fluctuates (up to 25 per cent), and its long term average may be significantly lower than its present-day value (Grigné *et al.* 2005; Labrosse & Jaupart, 2007). Similarly, 2-D Cartesian experiments with large aspect ratio and evolving plate boundaries exhibit strong variations in surface and basal heat flux (Gait & Lowman, 2007).

7 DISCUSSION AND CONCLUSIONS

Trade-offs between the parameters of eq. (20) for bottom heating and eq. (24) for mixed heating indicate that there is not a unique solution explaining our numerical experiments of thermal convection in a spherical shell. The minimum χ^2 solutions significantly differ from those predicted by TBL analysis. In the case of bottom heating, a solution with a temperature exponent equal to 4/3 fits our calculations well, but the Rayleigh number exponent is still smaller than 1/3, as is also the case in 3-D Cartesian studies. These discrepancies may be due to the fact that the top and bottom TBLs are interacting with one another, that is, that the heat transfer in the bottom (top) TBL is described by the superposition of TBL instabilities and of slab (plume) arrivals (Labrosse, 2002; Moore, 2008). The change in the vertical velocity structure with increasing fraction of basal heating observed by Choblet & Parmentier (2009) and its consequences on the temperature drop across the top TBL further illustrates the importance of plume/TBL interactions. In spherical geometry, the role of these interactions, relative to that of the TBL instabilities, is enhanced because of the geometrical asymmetry between the top and bottom TBLs. Deviations from the TBL analysis may also be related to the fact that the aspect ratio of the flow pattern changes with curvature and Rayleigh number. Because the Nusselt number slightly depends on the aspect ratio (Jarvis *et al.* 1995; Ratcliff *et al.* 1996; Grigné *et al.* 2005), one different scaling law should be designed for each aspect ratio, or the aspect ratio should be a parameter of the scaling law. Our scaling laws, however, do not explicitly depend on the aspect ratio of the flow pattern. The fact that we try to fit all our experiments using a single scaling law may partly explain the trade-offs we observe. Interestingly, differences between the scaling laws for each aspect ratio are small (Ratcliff *et al.* 1996), and overall the solutions we propose explain our calculations and those from previous studies very well. From that point of view, our scaling laws can be understood as empirical descriptions of heat transfer through an isoviscous spherical shell, and may thus be used to study the influence of curvature on heat transfer.

Viscous flows in planetary mantles include more complexities than the case of an isoviscous fluid studied in this paper. The thermal viscosity ratio is an essential ingredient for planetary mantle dynamics and heat transfer, a major effect of temperature-dependent viscosity being to reduce the heat transfer through the planetary mantles. The stagnant lid regime, obtained for large viscosity ratios, yields a Rayleigh number exponent of the heat flux scaling law between 0.20 and 0.26, depending on the study (Christensen, 1984; Moresi & Solomatov, 1995; Deschamps & Sotin, 2000). This regime is suitable in the case of monoplate planets, for example, Venus (Solomatov & Moresi, 1996), and icy moons of giant planets (Deschamps & Sotin, 2001), but is unrealistic in the case of the Earth, since it would prevent plate tectonics.

A key ingredient in the case of the Earth is plate tectonics. Plate tectonics may modify the mantle flow pattern, including changes in the aspect ratio, with the consequence that simple scaling laws cannot properly model the thermal evolution of the mantle (Grigné *et al.* 2005; Gait & Lowman, 2007; Labrosse & Jaupart, 2007). Another parameter that may play a significant role in the case of the Earth, is the presence of chemical heterogeneities at the bottom of the mantle, as mapped by normal modes (Trampert *et al.* 2004). Numerical models of thermochemical convection have shown that chemical layering at the CMB plays an important role in reducing core cooling (Nakagawa & Tackley, 2004a, 2005a). Similarly, the survival of large pools of dense primitive material, as observed in other numerical models (McNamara & Zhong, 2004; Deschamps & Tackley, 2008, 2009) may have an influence on the average and distribution in heat flux at the bottom of the mantle, and on the heat transfer through the mantle layer. Furthermore, if these reservoirs are richer than the regular mantle in radiogenic elements (Kellogg *et al.* 1999), the present-day Urey ratio may be higher than what is usually estimated (Korenaga, 2008).

Our models and scaling relationships also do not account for the presence of phase transition(s) in planetary mantles. In the case of the Earth, the endothermic phase transition to perovskite and ferro-periclase strongly modifies the flow pattern by reducing the mass exchange between the upper and lower mantles (e.g. Machetel & Weber, 1991; Tackley *et al.* 1993). In thermochemical models

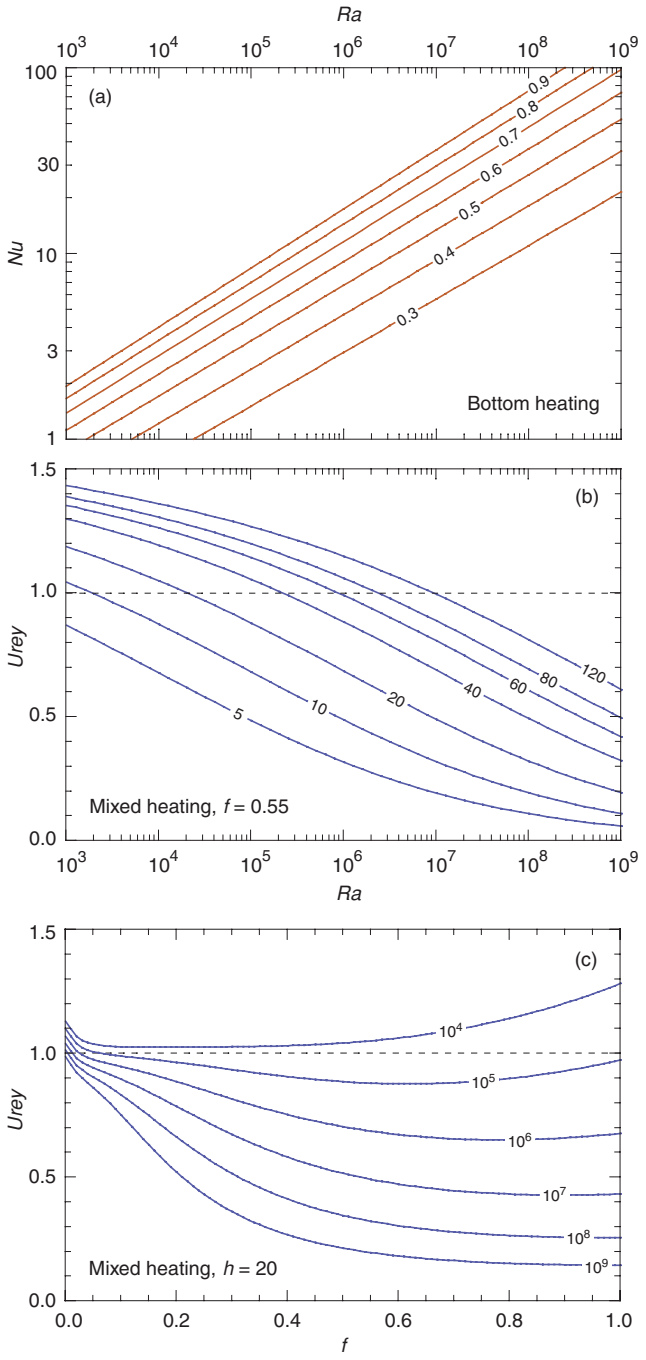

Figure 9. Influence of the curvature and the fraction of internal heating on the heating power transferred by convection through an isoviscous spherical shell. (a) Nusselt number as a function of the Rayleigh number, and for various values of f (labels on curves), in the case of bottom heating (eq. 20 and the minimum χ^2 values of inverted parameters). (b) Urey ratio as a function of the Rayleigh number, and for $f = 0.55$ and various values of the non-dimensional rate of internal heating (labels on curves), in the mixed heating case (eq. 24 and the minimum χ^2 values of inverted parameters). (c) Urey ratio as a function of curvature, and for $h = 20$ and various values of the Rayleigh number (labels on curves), in the mixed heating case (eq. 24 and the minimum χ^2 values of inverted parameters).

that include an initial layer of dense material (Deschamps & Tackley, 2009) a 660-km phase transition with a Clapeyron slope of -2.5 MPa K^{-1} strongly inhibits the rise of dense material above the phase transition and reduces the surface heat flux by about 40 per cent. Depending on Mars' core radius, which remains poorly constrained, the phase transition from ringwoodite to perovskite and magnesio-wüstite may be present or not in the Martian mantle. If present, the layer of perovskite and magnesio-wüstite would be thin (200 km at most), which may result in a decrease in the number of hot rising plumes and in the efficiency of mantle and core cooling (Breuer *et al.* 1998; Harder, 1998). In addition, 2-D-cylindrical calculations of van Thienen *et al.* (2006) showed that strong localized upwellings can be generated from a thin layer of perovskite. In the case of the Earth, the phase transition to post-perovskite (Murakami *et al.* 2004; Oganov & Ono, 2004) may also influence the mantle dynamics, and thus the heat transfer through the Earth's mantle (Nakagawa & Tackley, 2004b, 2005b).

Heat transfer through the Earth's mantle thus requires one to account for more complexities than curvature and volumetric heating. Performing full studies and deriving scaling laws in spherical geometry for these parameters is however beyond the scope of this paper.

Due to the limitations discussed above, the scaling relationships derived in this paper may not be well suited to describe heat transfer through the Earth's mantle. However, they provide a good description of the influence of curvature on the heat transfer through planetary mantles. Furthermore, they may be useful to model the thermal history of icy moons of giant planets. An interesting finding is that in the case of mixed heating, there exists an optimal curvature for which the Urey ratio reaches a minimum, and whose value is decided by the competition between the radiogenic power and the predicted convective heat flow. Next steps should focus on building scaling laws for other parameters, most importantly the thermal viscosity ratio, and on combining scaling relationships obtained for different modes of convection to model the thermal history of the Earth's mantle.

ACKNOWLEDGMENTS

We are grateful to Gaël Choblet, Julian Lowman, an anonymous colleague, and the editor (Stéphane Labrosse) for their detailed and constructive reviews and comments, which helped to improve the first version of this article. This research was funded by the Swiss National Science Foundation, grant 200021-111870. All numerical experiments were performed on the ETH's Linux supercluster Brutus.

REFERENCES

Behounkova, M. & Choblet, G., 2009. Onset of convection in a basally heated spherical shell, application to planets, *Phys. Earth planet. Inter.*, **176,** 157–173.

Breuer, D., Yuen, D.A., Spohn, T. & Zhang S., 1998. Three dimensional models of Martian mantle convection with phase transitions, *Geophys. Res. Lett.*, **25,** 229–232.

Chandrasekhar, S., 1961. *Hydrodynamic and Hydromagnetic Stability*, pp. 652 , Clarendon Press, New York.

Choblet, G. & Sotin, C., 2000. 3D thermal convection with variable viscosity: can transient cooling be described by a quasi-static scaling law? *Phys. Earth planet. Inter.*, **119,** 321–336.

Choblet, G. & Parmentier, E.M., 2009. Thermal convection heated both volumetrically and from below: implications for predictions of planetary evolution, *Phys. Earth planet. Inter.*, **173,** 290–296.

Christensen, U.R., 1984. Heat transport by variable viscosity convection and implications for the Earth's thermal evolution, *Phys. Earth planet. Int.*, **35,** 264–282.

Daly, S.F., 1980. Convection with decaying heat sources: constant viscosity, *Geophys. J. R. astr. Soc.*, **61,** 519–547.

Davies, G.F., 1980. Thermal history of convective Earth models and constraints on radiogenic heat production in the Earth, *J. geophys. Res.*, **85,** 2517–2530.

Deschamps, F. & Sotin, C., 2000. Inversion of two-dimensional numerical convection experiments for a fluid with a strongly temperature-dependent viscosity, *Geophys. J. Int.*, **143,** 204–218.

Deschamps, F. & Sotin, C., 2001. Thermal convection in the outer shell of large icy satellites, *J. geophys. Res.*, **106,** 5107–5121.

Deschamps, F. & Tackley, P.J., 2008. Searching for models of thermo-chemical convection that explain probabilistic tomography I – Principles and influence of rheological parameters, *Phys. Earth planet. Inter.*, **171,** 357–373.

Deschamps, F. & Tackley, P.J., 2009. Searching for models of thermo-chemical convection that explain probabilistic tomography II – Influence of physical and compositional parameters, *Phys. Earth planet. Inter.*, **176,** 1–18.

Dumoulin, C., Doin, M.-P. & Fleitout, L., 1999. Heat-transport in stagnant lid convection with temperature- and pressure-dependent Newtonian or non-Newtonian rheology, *J. geophys. Res.*, **104,** 12 759–12 777.

Gait, A.D. & Lowman, J.P., 2007. Time-dependence in mantle convection models featuring dynamically evolving plates, *Geophys. J. Int.*, **171,** 463–477.

Grigné, C., Labrosse, S. & Tackley, P.J., 2005. Convective heat transfer as a function of wavelength: implications for the cooling of the Earth, *J. geophys. Res.*, **110,** B3409, doi:10.1029/2004JB003376.

Harder, H., 1998. Phase transition and three-dimensional planform of thermal convection in Martian mantle, *J. geophys. Res.*, **103,** 16 775–16 797.

Hernlund, J. & Tackley, P.J. 2008. Modeling mantle convection in the spherical annulus, *Phys. Earth planet. Inter.*, **171,** 48–54.

Howard, L.N., 1966. Convection at high Rayleigh number, in *Proceedings of the 11th International Congress on Applied Mechanics*, pp. 1109–1115, eds Gortler, H., Springer-Verlag, New-York.

Iwase, Y. & Honda, S., 1998. Effect of geometry on the convection with core-cooling, *Earth Planets Space*, **50,** 387–395.

Jarvis, G.T. & Peltier, W.R., 1982. Mantle convection as a boundary layer phenomenon, *Geophys. J. R. astr. Soc.*, **68,** 389–427.

Jarvis, G.T., Glatzmaier, G.A. & Vangelov, V.I., 1995. Effect of curvature, aspect ratio, and planform in two- and three-dimensional spherical models of thermal convection, *Geophys. astrophys. Fluid Dyn.*, **79,** 147–171.

Kageyama, A. & Sato, T., 2004. "Yin-Yang grid": an overset grid in spherical geometry, *Geochem. Geophys. Geosyst.*, **5,** Q09005, doi:10.1029/2004GC000734.

Kellogg, L.H., Hager, B.H. & Van Der Hilst, R.D., 1999. Compositional stratification in the deep mantle, *Science*, **283,** 1881–1884.

Khan, A. & Connolly, J.A.D., 2008. Constraining the composition and thermal state of Mars from inversion of geophysical data, *J. geophys. Res.*, **113,** E07003, doi:10.1029/2007JE002996.

Korenaga, J., 2008. Urey ratio and the structure and evolution of Earth's mantle, *Rev. Geophys.*, **46,** RG2007, doi:10.1029/2007RG000241.

Krishnamurti, R., 1968. Finite amplitude convection with changing mean temperature. Part 1. Theory, *J. Fluid Mech.*, **33,** 445–455.

Labrosse, S., 2002. Hotspots, mantle plumes, and core heat loss, *Earth planet. Sci. Lett.*, **199,** 147–156.

Labrosse, S. & Jaupart, C., 2007. Thermal evolution of the Earth: secular changes and fluctuations of plate characteristic, *Earth planet. Sci. Lett.*, **260,** 465–481.

Lenardic, A., Moresi, L., 2003. Thermal convection below a conducting lid of variable extent: heat flow scaling and two-dimensional, infinite Prandtl number numerical simulations, *Phys. Fluids*, **15,** 455–466.

Machetel, P. & Weber, P., 1991. Intermittent layered convection in a model mantle with an endothermic phase change at 670 km, *Nature*, **350,** 55–57.

McKenzie, D.P, Roberts, J.M. & Weiss, N.O., 1974. Convection in the Earth's mantle: towards a numerical simulation, *J. Fluid. Mech.*, **62,** 465–538.

McNamara, A. K. & Zhong, S., 2004. Thermochemical structures within a spherical mantle. *J. geophys. Res.*, **109,** doi:10.1029/2003JB00287.

McNamara, A.K. & Zhong, S., 2005. Degree-one mantle convection: dependence on internal heating and temperature-dependent rheology, *Geophys. Res. Lett.*, **32,** doi:10.1029/2004GL021082.

Moore, B., 2008. Heat transport in a convective layer heated from within and below, *J. geophys. Res.*, **113,** B11407, doi:10.1029/2006JB004778.

Moore, D.R. & Weiss, N.O., 1973. Two-dimensional Rayleigh-Bénard convection, *J. Fluid Mech.*, **58,** 289–312.

Moresi, L.-N. & Solomatov, V.S., 1995. Numerical investigation of 2-D convection with extremely large viscosity variations, *Phys. Fluids*, **7,** 2154–2162.

Murakami, M., Hirose, K., Kawamura, K., Sata, N. & Ohishi, Y., 2004. Post-perovskite phase transition in $MgSiO_3$, *Science*, **304,** 855–858.

Nakagawa, T. & Tackley, P.J., 2004a. Effects of thermo-chemical convection on the thermal evolution of the Earth's core, *Earth planet. Sci., Lett.*, **220,** 207–219.

Nakagawa, T. & Tackley, P.J., 2004b. Effects of a perovskite-post perovskite phase change near the core-mantle boundary on compressible mantle convection, *Geophys. Res. Lett.*, **31,** doi:10.1029/2004GL020648.

Nakagawa, T. & Tackley, P.J., 2005a. Deep mantle heat flow and thermal evolution of Earth's core in thermo-chemical multiphase models of mantle convection, *Geochem. Geophys. Geosyst.*, **6,** doi:10.1029/2005GC000967.

Nakagawa, T. & Tackley, P.J., 2005b. The interaction between the post-perovskite phase change and a thermo-chemical boundary layer near the core-mantle boundary, *Earth planet. Sci., Lett.*, **238,** 204–216.

Oganov, A.R. & Ono, S., 2004. Theoretical and experimental evidence for a post-perovskite phase of $MgSiO_3$ in Earth's D" layer, *Nature*, **430,** 445–448.

Ratcliff, J.T., Schubert, G. & Zebib, A., 1996. Steady tetrahedral and cubic patterns of spherical shell convection with temperature-dependent viscostity, *J. geophys. Res.*, **101,** 25 473–25 484.

Reese, C.C., Solomatov, V.S., Baumgardner, J.R. & Yang, W.-S., 1999. Stagnant lid convection in a spherical shell, *Phys. Earth planet. Inter.*, **116,** 1–7.

Reese, C.C., Solomatov, V.S. & Baumgardner, J.R., 2005. Scaling laws for time-dependent stagnant lid convection in a spherical shell, *Phys. Earth planet. Inter.*, **149,** 361–370.

Schubert, G. & Anderson, C.A., 1985. Finite element calculations of very high Rayleigh number thermal convection, *Geophys. J. R. astr. Soc.*, **80,** 575–601.

Schubert, G., Cassen, P. & Young, R.E., 1979. Subsolidus convective cooling histories of terrestrial planets, *Icarus*, **38,** 192–211.

Schubert, G., Bercovici, D. & Glatzmaier, G.A., 1990. Mantle dynamics in Mars and Venus: influence of an immobile lithosphere on three-dimensional mantle convection, *J. geophys. Res.*, **95,** 14 105–14 129.

Shahnas, M.H., Lowman, J.P., Jarvis, G.T. & Bunge, H.-P., 2008. Convection in a spherical shell heated by an isothermal core and internal sources: implication for the thermal state of planetary mantles, *Phys. Earth planet. Inter.*, **168,** 6–15.

Sharpe, H. & Peltier, W.R., 1978. Parameterized mantle convection and the Earth's thermal history, *Geophys. Res. Lett.*, **5,** 737–740.

Smolarkiewicz, P.K., 1984. A fully multidimensional positive definite advection transport algorithm with small implicit diffusion, *J. Comput. Phys.*, **54,** 325–362.

Solomatov, V.S. & Moresi, L.-N., 1996. Stagnant lid convection on Venus, *J. geophys. Res.*, **101,** 4737–4753.

Sotin, C., 1986. *Contribution à l'étude de la structure et de la dynamique interne des planètes*, pp.385, Thèse de l'Université Paris VII, Paris.

Sotin, C. & Labrosse, S., 1999. Three-dimensional thermal convection in an iso-viscous, infinite Prandtl number fluid heated from within and from below: application to the transfer of heat through planetary mantles, *Phys. Earth planet. Inter.*, **112,** 171–190.

Stevenson, D.J., Spohn, T. & Schubert, G., 1983. Magnetism and thermal evolution of terrestrial planets, *Icarus*, **54,** 466–489.

Stüben, K. & Trottenberg, U., 1982. Multigrid method: fundamental algorithms, model problem analysis and applications, in *Multigrid Method*, pp. 1–175, eds Hackbusch, W. & Trottenberg, U., Springer-Verlag.

Tackley, P.J., Stevenson, D.J., Glatzmaier, G.A. & Schubert, G., 1993. Effect of an endothermic phase transition at 670 km in a spherical model of convection in the Earth's mantle, *Nature*, **361,** 699–704.

© 2010 The Authors, *GJI*, **182,** 137–154
Journal compilation © 2010 RAS

Tackley, P.J., 1998. Three-dimensional simulations of mantle convection with a thermo-chemical CMB boundary layer: D"? in *The Core-Mantle Boundary Region*, *Geodynamical Ser 28*., pp. 231–253, eds Gurnis, M. *et al*., AGU, Washington, DC.

Tackley, P.J., 2008. Modelling compressible mantle convection with large viscosity contrasts in a three-dimensional spherical shell using the yin-yang grid, *Phys. Earth planet. Inter.*, **171,** 7–18.

Tarantola, A. & Valette, B., 1982. Generalized nonlinear inverse problems solved using the least square criterion, *Rev. Geophys. Space Phys.*, **20,** 219–232.

Trampert, J., Deschamps, F., Resovsky, J.S. & Yuen, D.A., 2004. Probabilistic tomography maps significant chemical heterogeneities in the lower mantle, *Science*, **306,** 853–856.

Travis, B., & Olson, P., 1994. Convection with internal sources and turbulence in the Earth's mantle, *Geophys. J. Int.*, **118,** 1–19.

Turcotte, D.L., & Schubert, G., 1982. *Geodynamics: Application of Continuum Physics to Geological Problems*, pp. 450, John Wiley & Sons, New York.

Vangelov, V.I. & Jarvis, G.T., 1994. Geometrical effects of curvature in axisymmetric spherical models of mantle convection, *J. geophys. Res.*, **99,** 9345–9358.

van Thienen, P., Rivoldini, A., van Hoolst, T. & Lognonné, P., 2006. A top-down origin for the martian mantle plumes, *Icarus*, **185,** 197–210.

Wolstencroft, M., Davies, J.H. & D.R. Davies, D.R., 2009. Nusselt-Rayleigh scaling for spherical shell Earth mantle simulation up to a Rayleigh number of 10^9, *Phys. Earth planet. Inter.*, **176,** 132–141.

Zebib, A., Schubert, G., Dein, J.L. & Paliwal, R.C., 1983. Character and stability of axisymmetric thermal convection in spherical shells, *Geophys. astrophys. Fluid Dyn.*, **23,** 1–42.

APPENDIX A: INVERSION'S *A POSTERIORI* ANALYSIS

Throughout this study, we used the non-linear generalized inverse method of Tarantola & Valette (1982) to invert our observations for the parameters of the scaling laws following a theoretical model (e.g. in this study, eqs. 16 or 23 for temperature or eqs 20 or 24 for heat flux). This iterative process is initiated by prescribing some *a priori* knowledge on the parameters (approximate values, and *a priori* error bars to search in). The inverse matrix is built from the *a priori* covariance matrix (built from the uncertainties in the observed data and the *a priori* uncertainties in the parameters) and the matrix of the partial derivatives of the theoretical model. These derivatives are recalculated at each iteration of the process. The iterative process is stopped when the solution (parameter values) is stationary. In addition to the parameter values, the inversion provides an *a posteriori* covariance matrix,

$$\mathbf{C} = \mathbf{C}_0 - \mathbf{C}_0 \cdot \mathbf{F^T} \cdot \left(\mathbf{F} \cdot \mathbf{C}_0 \cdot \mathbf{F^T}\right)^{-1} \cdot \mathbf{F} \cdot \mathbf{C}_0, \tag{A1}$$

where $\mathbf{C}_0$ is the *a priori* covariance matrix, and F is the matrix of partial derivatives at the last iteration of the inversion. Uncertainty σ_p^j in the jth parameter is calculated from the jth diagonal element of the covariance matrix,

$$\sigma_p^j = \sqrt{C_{jj}}. \tag{A2}$$

The *a posteriori* analysis designed by Sotin (1986) allows an estimation of the quality of the inversion. A first indicator is the distribution of the difference between the observed and modelled data relative to the observed uncertainties in the data,

$$e_d^i = \frac{\left(d_{\rm mod}^i - d_{\rm obs}^i\right)}{\sigma_{\rm obs}^i}, \tag{A3}$$

where $d_{\rm obs}^i$ and $d_{\rm mod}^i$ are the ith observed and modelled data, and $\sigma_{\rm obs}^i$ is the observed uncertainty on ith observed data. Uncertainties originate both from small inaccuracies in the calculations (which can be estimated from convergence tests) and, for quasi-stationary cases, small oscillations around the average solution. Here, we assumed a 3 per cent error on the Nusselt number and on the average temperature for calculations listed in Tables 1 and 2 which is a conservative estimate. The better the inversion, the closer its distribution in e_d to a Gaussian distribution centred around the zero value. Histograms in Fig. A1 show the distributions obtained for the heat flux scaling laws discussed in this study. The minimum χ^2 solutions obtained for bottom heating (Fig. A1a) and mixed heating (Fig. A1c) explain well the observed data sets. In addition, the solution obtained for bottom heating and $c = 1.33$ (Fig. A1b) also explains well bottom heating data. By contrast, the solutions obtained for the joint inversion of bottom heated and mixed heated cases show strong dispersion in e_d (Figs A1e and f), indicating that these inversions fail to simultaneously explain the bottom heating and mixed heating observations.

Second, the χ^2 function, which sums up the difference between the observed and modelled data relatively to the uncertainties in the observed data,

$$\chi^2 = \sum_{i=1}^{N} \frac{\left(d_{\rm mod}^i - d_{\rm obs}^i\right)^2}{{\sigma_{\rm obs}^i}^2}, \tag{A4}$$

provides a good indication of the quality of the inversion. Inversion is considered as good if $\chi^2 \leq 2N$, where N is the number of data. The χ^2 obtained for the inversion performed in this study are listed in Table 3. The inversion process leads to the set of parameters that minimizes the χ^2. However, depending on the presence of trade-offs between the inverted parameters, several sets of parameter may satisfy the condition $\chi^2 \leq 2N$, and explain observations within their error bar.

Finally, the off-diagonal elements of covariance matrix indicate possible trade-off between the inverted parameters. Ideally, if the parameters i and j are independent, the diagonal element C_{ij} should be equal to zero. The normalized element,

$$\tilde{C}_{ij} = \frac{C_{ij}}{\sqrt{\sigma_p^i \sigma_p^j}}, \tag{A5}$$

measures the degree of correlation between parameters i and j. The correlation (anticorrelation) between the parameters i and j increases as $\tilde{C}_{ij}$ gets closer to 1 (-1). In this study, inversions of the observed surface heat flux for bottom heating (Table 1) following eq. (20) indicate substantial trade-off between the parameters of this relationship. Moderate trade-offs between the parameters of the heat flux scaling for mixed heating (eq. 24) are also present.

APPENDIX B: MINIMUM UREY RATIO

The scaling laws we inferred for mixed heating (eqs 23 and 24) predict that given the Rayleigh number Ra and the non-dimensional rate of internal heating h, the Urey ratio reaches a minimum for a ratio f_0 of the core to total radii (Fig. 9c). The position of this minimum depends on Ra and h, and can be calculated by deriving eq. (26) with respect to f:

$$\frac{\partial Ur}{\partial f} = \frac{h}{3Nu_{\rm top}} \left[(1+2f) - \left(1+f+f^2\right) \frac{\partial \ln\left(Nu_{\rm top}\right)}{\partial f} \right], \tag{B1}$$

where $Nu_{\rm top}$ is given by eq. (24) and

$$\frac{\partial Nu_{\rm top}}{\partial f} = Nu_{\rm top} \left[\frac{a_2}{f} + b_2 \ln(Ra) + c \frac{\partial \ln(\theta_H)}{\partial f} \right] \tag{B2}$$

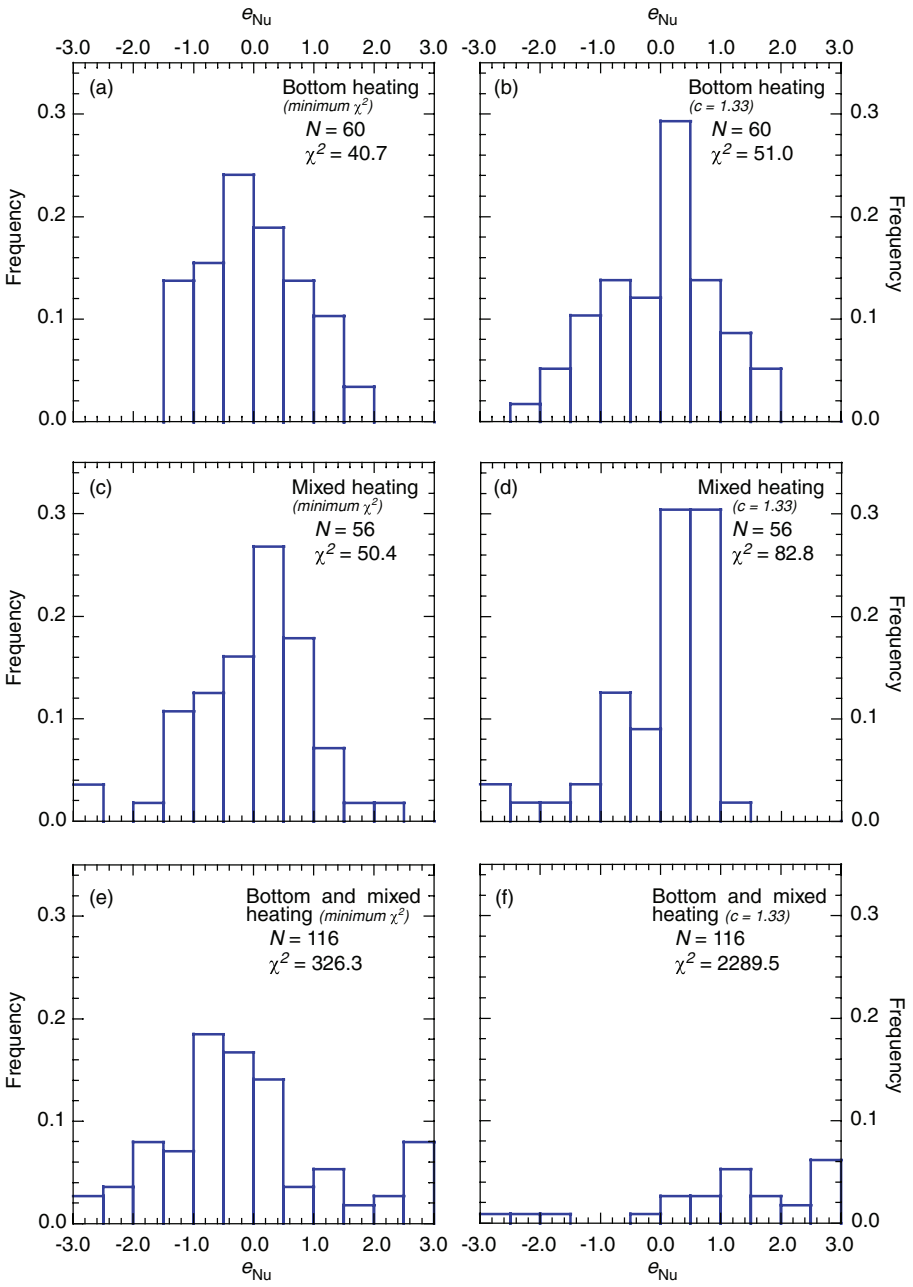

Figure A1. Normalized frequency of the relative error (eq. A3) in non-dimensional surface heat flux. (a) Inversion of bottom heating data (Table 1) following eq. (20), minimum χ^2 solution. (b) Inversion of bottom heating data (Table 1) following eq. (20) with c fixed to 1.33. (c) Inversion of mixed heating data (Table 2) following eq. (24), minimum χ^2 solution. (d) Inversion of mixed heating data (Table 2) following eq. (24) with c fixed to 1.33. (e) Simultaneous inversion of bottom heating and mixed heated data following eq. (24), minimum χ^2 solution. (f) Simultaneous inversion of bottom heating and mixed heated data following eq. (24) with c fixed to 1.33.

$$\frac{\partial \theta_H}{\partial f} = \frac{\partial \theta_m}{\partial f} + \left(\frac{1+f+f^2}{3}\right)^{\beta} \times \frac{h^{\beta}}{Ra^{\gamma}} \left[\alpha_2 + (\alpha_1 + \alpha_2 f)\frac{\beta\,(1+2f)}{(1+f+f^2)}\right] \tag{B3}$$

$$\frac{\partial \theta_m}{\partial f} = \frac{\alpha \beta_1 f^{(\beta_1 - 1)}}{\left[1 + (2\alpha - 1)\, f^{\beta_2}\right]^2} \tag{B4}$$

We solved eq. (B1) using a Newton–Raphson method and values of the parameters obtained for the minimum χ^2 solutions of our inversions (Table 3), that is, $\alpha = 1.0$, and $\beta_1 = \beta_2 = 2.0$ for θ_m, $\alpha_1 = 1.68$, $\alpha_1 = -0.8$, $\beta = 0.779$ and $\gamma = 0.234$ for θ_H and $a_1 = 0.59$ $a_2 = 0.05$, $b_1 = 0.3$, $b_2 = -0.003$, $c = 1.23$ for $Nu_{\rm top}$. Results are shown in Fig. B1, which indicates that f_0 increases with Ra, and decreases with increasing h. (Fig. B1a), and that the minimum Urey ratio increases with h and decreases with increasing Ra (Fig. B1b).

© 2010 The Authors, *GJI*, **182,** 137–154
Journal compilation © 2010 RAS

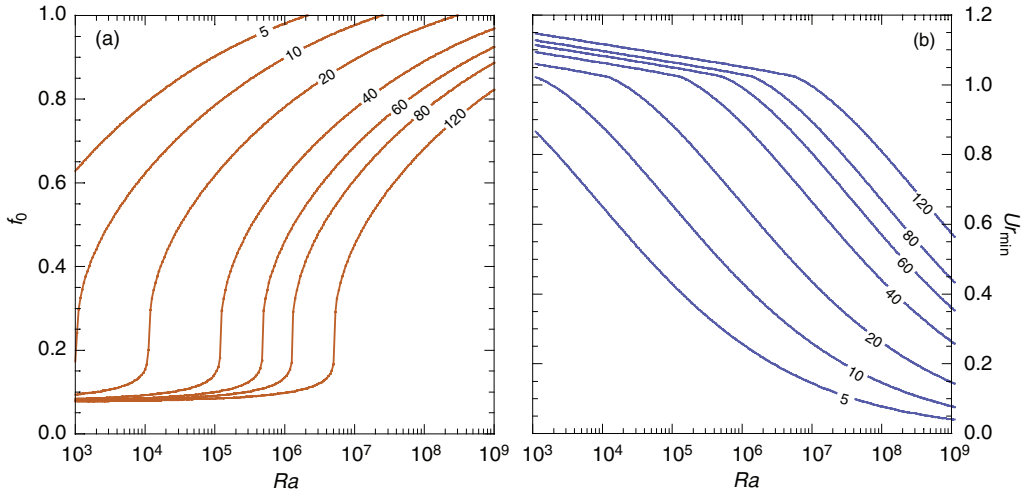

Figure B1. (a) Ratio f_0 of the core-to-total radii at the minimum Urey ratio, calculated by solving eq. (B1). Results are presented as a function of the Rayleigh number and for several values of the non-dimensional rate of internal heating (labels on curves). (b) Minimum Urey ratio as a function of Rayleigh number, and for several values of the non-dimensional rate of internal heating (labels on curves).